universität wien

MASTERARBEIT | MASTER'S THESIS

Titel | Title

Large area holographic gratings in nanodiamond-polymer composites for neutron interferometry

verfasst von | submitted by

Roxana Helena Ackermann BSc

angestrebter akademischer Grad | in partial fulfilment of the requirements for the degree of

Master of Science (MSc)

Wien | Vienna, 2026

Studienkennzahl lt. Studienblatt | Degree programme code as it appears on the student record sheet:	UA 066 876
Studienrichtung lt. Studienblatt | Degree programme as it appears on the student record sheet:	Masterstudium Physics
Betreut von | Supervisor:	ao. Univ.-Prof. Dr. Martin Fally

Acknowledgements

At this point, I would like to express my sincere gratitude to all those who supported and accompanied me during the preparation of this master's thesis.

My special thanks go to ao. Univ.-Prof. Dr. Martin Fally, who supervised and evaluated this thesis. Through his continuous support and his always open approach to discussion, I had the opportunity to clarify questions and address scientific problems at any time. His supervision was essential for the successful completion of this thesis and enabled me to carry out the experimental work in a structured, productive and motivating environment, making the time spent in the laboratory both effective and enjoyable. In this context, I would also like to thank Dipl.-Ing. Dr. Jürgen Klepp, who was always available to answer questions and provided substantial support, particularly during the chemical laboratory work. Through his guidance, patience and scientific expertise, I was able to resolve many issues and make decisive progress in my work. I also thank Mag. Dr. Christian Pruner from the University of Salzburg for his helpful feedback and valuable suggestions during the laboratory work.

Furthermore, I would like to thank my fellow students for their helpfulness throughout my studies, for the scientific exchange and for their interest in my work, as well as for the many supportive discussions. I also thank my friends, who provided emotional support and encouragement and carried me through this time.

Finally, I would like to express my sincere gratitude to my family. I am particularly grateful to my parents for their continuous support, especially their financial support, which made my studies at the University of Vienna possible in the first place and significantly eased my academic path. My deepest gratitude goes to my sister Priscilla, who accompanied me throughout this entire period with great care. She always had an open ear, was available at all times and provided emotional support and encouragement during difficult phases. I would also like to express my sincere gratitude to my brother-in-law Martin for his constant encouragement and for always being there for me whenever I needed support. The continuous support of my family was essential for the successful completion of this thesis.

Abstract

This Master's thesis entitled "Large-area holographic gratings in nanodiamond–polymer composites for neutron interferometry" focuses on the fabrication of large-area, homogeneous and high-quality nanodiamond–polymer composite (NDPC) volume gratings for applications in neutron interferometry. The gratings are fabricated by holographic recording and subsequently characterised by optical diffraction. The aim of this work is the preparation of three volume gratings for use in a very cold neutron (VCN) interferometer in LLL (triple-Laue) geometry, where two gratings are intended to act as beam splitters and one grating as a mirror element. The interferometer is being implemented at the PF2 VCN beamline at the Institut Laue-Langevin (ILL) in Grenoble. The thesis describes the fabrication of the NDPC starting material, the preparation of the NDPC samples and the holographic recording of the gratings using a two-beam setup. The optical characterisation is performed by angle-dependent diffraction efficiency measurements in the form of rocking curves. The analysis of the experimental data is based on coupled-wave theory according to Uchida. The gratings are recorded sequentially under identical conditions on a highly planar granite bench and are aligned with microradian precision using an autocollimator to ensure exact parallelism of the grating vectors with respect to each other as well as relative to the surface of the respective glass substrate. At the ILL, the three gratings constituting the VCN interferometer are aligned in an identical manner on an equally highly planar granite bench using the autocollimator. The objective is to achieve a high refractive index modulation, a laterally homogeneous grating thickness and a high diffraction efficiency for very cold neutrons. The results show that these requirements are successfully fulfilled. The fabricated NDPC gratings therefore meet the essential prerequisites for their use in an LLL neutron interferometer for very cold neutrons.

Kurzfassung

Diese Arbeit mit dem Titel „Large area holographic gratings in nanodiamond–polymer composites for neutron interferometry“ befasst sich mit der Herstellung großflächiger, homogener und hochqualitativer Nanodiamant-Polymer-Komposit-Volumengitter (NDPC) für die Anwendung in der Neutroneninterferometrie. Die Gitter werden mittels holographischer Aufzeichnung hergestellt und anschließend durch Lichtbeugung optisch charakterisiert. Ziel der Arbeit ist die Vorbereitung von drei Volumengittern für den Einsatz in einem Very-Cold-Neutron Interferometer (VCN) in LLL-Geometrie (triple Laue), wobei zwei Gitter als Strahlteiler und ein Gitter als Spiegel vorgesehen sind. Das Interferometer wird an der PF2-VCN-Beamline am Institut Laue-Langevin (ILL) in Grenoble aufgebaut. Die Arbeit beschreibt die Herstellung des NDPC-Ausgangsmaterials, die Präparation der NDPC-Proben sowie die holographische Aufzeichnung der Gitter in einem Zwei-Strahl-Aufbau. Die optische Charakterisierung erfolgt anhand winkelabhängiger Beugungseffizienzmessungen in Form von Rocking Kurven. Die Analyse der Messergebnisse basiert auf der Coupled-Wave-Theory nach Uchida. Die Gitter werden nacheinander unter identischen Bedingungen auf einer hochplanaren Granitbank aufgezeichnet und mithilfe eines Autokollimators mit mikroradianer Präzision ausgerichtet, um eine exakte Parallelität der Gittervektoren zueinander sowie relativ zur Oberfläche des jeweiligen Glassubstrats sicherzustellen. Am ILL werden die drei Gitter, die das VCN-Interferometer bilden, in identischer Weise auf einer ebenso hochplanaren Granitbank mithilfe des Autokollimators ausgerichtet. Ziel ist es, eine hohe Brechungsindexmodulation, eine laterale Homogenität der Gitterdicke sowie eine hohe Beugungseffizienz für sehr kalte Neutronen zu erreichen. Die Ergebnisse zeigen, dass diese Anforderungen erfolgreich erfüllt werden konnten. Die hergestellten NDPC-Gitter erfüllen damit die wesentlichen Voraussetzungen für ihren Einsatz in einem LLL-Neutroneninterferometer für sehr kalte Neutronen.

Contents

List of Tables

List of Figures

1. Introduction

Studying interference phenomena is considered one of the most interesting challenges in physics, since it enables fundamental questions of physics to be investigated and accurate measurements to be carried out [1]. Many of the phenomena well known from light optics can also be found in neutron optics and result from the wave-like properties of neutrons, their ability to interact with all four fundamental forces of nature and mathematical analogies seen in light optics [2]. Since the 1970s, classical optical experiments have been adapted for use in neutron optics, leading to significant and fascinating advances in neutron interferometry and the development of various types of neutron interferometers [2, 3]. This development began in 1962, when Maier-Leibnitz and Springer were the first to develop a neutron interferometer based on wavefront division and biprism deflection [4]. However, it could not be used for interferometric applications primarily because of small beam separation. Despite this limitation, the approach remained of interest for diffraction experiments on macroscopic objects [2]. In 1965, Bonse and Hart were the first to employ the amplitude division method in a perfect crystal interferometer for X-rays [5]. Later, the largest amplitude division for neutrons was realized by Rauch, Treimer and Bonse in 1974 [3]. They demonstrated the interference of two widely separated coherent beams of thermal neutrons using a perfect silicon crystal, whose perfect arrangement of lattice planes caused a coherent amplitude division by dynamical Bragg diffraction [2, 3]. This method has since become the standard technique for advanced neutron optical investigations [2]. Today, the importance of neutron interferometry is broad and ranges from its ability to accurately measure neutron scattering lengths and coherence properties, investigate materials, and support research and applications in quantum mechanics and gravitational studies [1, 6, 7].

While the perfect silicon crystal interferometer is limited to thermal neutrons, a different approach is needed for very cold neutrons [6, 8]. More precisely, Bragg diffraction can no longer occur once the wavelength of the colder neutrons exceeds twice the lattice plane spacing in crystals, leading to a sharp Bragg cutoff. Nevertheless, neutrons with such long wavelengths can still be diffracted using macroscopically structured materials such as artificially made gratings [2]. Such an interferometer for very cold neutrons (VCN) was realized in 2000 by van der Zouw et al., who implemented a neutron interferometer in triple-Laue (LLL) geometry at the Institut Laue-Langevin (ILL) based on microfabricated diffraction gratings, enabling interferometric experiments with very cold neutrons, including measurements of gravitational and Aharonov-Bohm phase shifts [9, 10]. Furthermore, this concept was further developed in 2006 by Pruner et al., who realized an LLL-type interferometer for cold neutrons using holographically generated volume gratings in photosensitive polymer materials [6].

Building on these developments, recent work has focused on holographically recorded volume gratings, which enable large, homogeneous diffraction elements with high quality, allowing larger VCN interferometers with increased phase sensitivity. The objective of this Master's thesis is to prepare gratings for such an interferometer for very cold neutrons. This is achieved by fabricating large-area, homogeneous and high-quality nanodiamond–polymer composite (NDPC) volume gratings using holographic recording and by characterising them using light diffraction under Bragg condition. Therefore, three NDPC volume gratings with target thicknesses of $d_0 \approx 25\,\mu$m and $d_0 \approx 50\,\mu$m are required, where two gratings serve as beam splitters and one as a mirror. All gratings should exhibit a well-defined and spatially uniform thickness d across the entire grating area, achieve a refractive index modulation of $n_{1,sat} \geq 0.01$ (see eq. 2.1), exhibit a high diffraction efficiency η (see eq. 2.3) and have identical grating periods of approximately $\Lambda = 500\,$nm. The gratings should be reproducibly fabricated with identical grating parameters and ultra-precisely parallel grating vectors in their recording positions. Angle-dependent diffraction efficiency measurements in the form of rocking curves are performed and analysed using coupled-wave theory according to Uchida [11]. From these measurements, the refractive index modulation n_1, effective grating thickness d, decay length L, coupling strength ν and diffraction efficiency η are extracted. The overall goal is to establish the prerequisites for application in an LLL interferometer at the PF2 VCN beamline at the Institut Laue-Langevin in Grenoble.

The thesis is organized as follows: the theoretical background is presented in Chapter 2, introducing the fundamental principles of diffraction in volume gratings, the coupled-wave theory of Kogelnik and Uchida, the operating principles of LLL interferometry and the mechanisms of grating formation in NDPCs. Chapter 3 describes the experimental setup and procedures in detail, including the chemical preparation of the NDPC material, sample fabrication, mounting and alignment of the gratings using an electronic autocollimator, as well as the holographic two-wave mixing recording process. The optical characterisation and results based on rocking curve measurements are presented in Chapter 4. Finally, Chapter 5 analyses the extracted grating parameters and discusses the comparison of the gratings and their suitability for the application in an LLL interferometer for very cold neutrons exhibiting a wavelength distribution with a peak at $\lambda_N \approx 4.5\,$nm and a full width at half maximum (FWHM) of $0.5\,$nm [12].

2. Theoretical Background

2.1. Diffraction from Volume Holographic Gratings

The fabrication of gratings for application in very cold neutron (VCN) interferometers can be achieved using holographic recording techniques. In the recording process a coherent, s-polarized laser beam with wavelength λ (vacuum) is divided into two plane waves of equal intensity $I_0/2$, that interfere inside a photosensitive medium [1]. The interference of these two recording beams, which enclose an angle 2Θ, creates a one-dimensional sinusoidal intensity modulation $\Delta I(x) \propto \cos(Kx)$, characterized by the spatial period $\Lambda = 2\pi/K$ [13]. This periodic illumination induces a spatially varying modulation of the complex refractive index $\tilde{n}(x)$ (or equivalently the permittivity) within the material, thereby forming a volume holographic diffraction grating [14]. For periodically modulated gratings, the imaginary part accounts for absorption, which is considered negligible in this work, while the real part corresponds to a pure phase grating with refractive index $n(x)$

$$n(x) = n_0 + \sum_{s=1}^{+\infty} \Delta n_s \cos(sKx + \varphi_s), \tag{2.1}$$

where

$$\Lambda = \frac{2\pi}{K} = \frac{\lambda}{2\sin\Theta} \tag{2.2}$$

is the grating spacing with the spatial frequency K along x, φ_s is the relative phase and n_0 is the average refractive index of the medium. Δn_s represents the refractive index modulation of order s and is related to the complex Fourier coefficients $\tilde{n}_s$ by $\Delta n_s = 2|\tilde{n}_s|$, where $|\tilde{n}_s| = n_s$ denotes the amplitude of the Fourier component of order s. The index s specifies the spatial harmonic of the periodic modulation, corresponding to the s-th Fourier component of the grating profile [15]. Figure 2.1 illustrates the recording geometry of the photosensitive medium leading to a periodic refractive-index modulation, as well as the subsequent optical characterization of the phase grating by light diffraction.

Holographic gratings can be characterized by diffraction experiments through the angular dependence of the diffraction efficiency $\eta(\Theta)$. Measuring the diffraction efficiency as a function of the angular deviation from the external Bragg angle Θ_B yields the so-called rocking curve [16]. In the Bragg regime, the diffraction efficiency is experimentally determined from the measured intensities of the diffracted and forward-diffracted beams as

$$\eta(\Theta) = \frac{I_D}{I_D + I_F}, \tag{2.3}$$

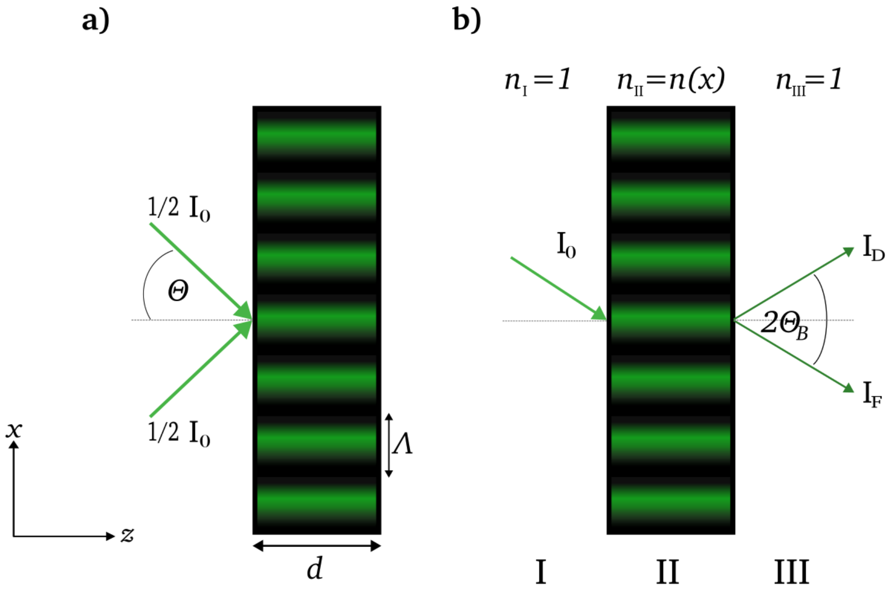

Figure 2.1.: Holographic recording and readout geometry of a volume phase grating. a) Recording process: two coherent plane waves interfere inside a photosensitive medium, forming a one-dimensional periodic refractive-index modulation $n(x)$. b) Bragg-Readout: an incident beam of intensity I_0 is diffracted into the forward-diffracted beam I_F and the diffracted beam I_D, separated by the angle $2\Theta_B$. (Own illustration, based on [16]).

where I_D and I_F denote the intensities of the diffracted and forward-diffracted beams, respectively [15, 16]. Maximum diffraction efficiency is obtained when the Bragg condition

$$2\Lambda \sin\Theta_B = m\lambda \tag{2.4}$$

is satisfied, where m is the diffraction order ($m = 1, 2, ...$) [17, 18]. The diffraction properties of a holographic grating are determined by the grating period Λ, the thickness d of the grating, the wavelength λ in vacuum used for recording and the Fourier composition of the refractive-index modulation, including the amplitudes Δn_s and relative phases φ_s [15]. Since higher diffraction orders strongly violate the Bragg condition and are severely attenuated, diffraction in thick volume gratings can be described by two-wave coupling, allowing the refractive-index modulation to be approximated by a single sinusoidal component [17], i.e. the first spatial harmonic ($s = 1$). A widely used theoretical framework for describing diffraction in thick volume holographic gratings are the two-coupled-wave theories introduced by Kogelnik and Uchida, which are described in the following chapter.

2.2. First-Order Coupled-Wave Theories

Kogelnik's coupled-wave theory (1969) provides a standard analytical description of Bragg diffraction in sinusoidal volume gratings [19]. In this theory, coupled-wave differential equations for the transmitted and first-order diffracted waves are derived and solved analytically, yielding expressions for the diffraction efficiency as well as its angular and wavelength dependence. An extension of Kogelnik's coupled-wave theory for diffraction by thick gratings was provided by Uchida (1973), who analyzed volume gratings with a depth-dependent refractive index modulation [11]. In this approach, the general solution of the coupled differential equations for the transmitted and first-order diffracted waves can be obtained by assuming an exponential decay of the refractive index modulation along the grating thickness (z-axis) with $n_1(z) = n_1(0) \exp(-z/L)$ [15].

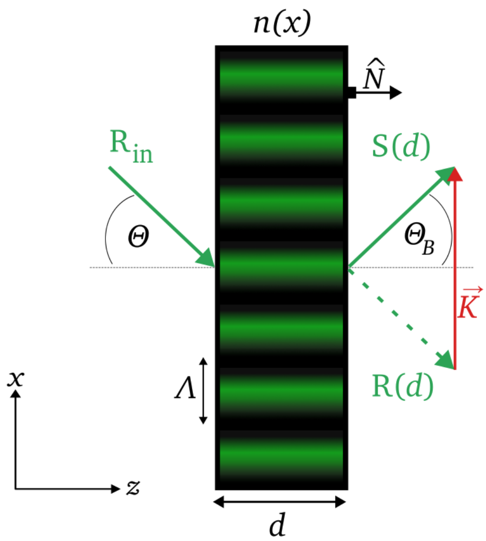

Figure 2.2.: Schematic of a holographic volume grating in transmission geometry with a spatially periodic modulation of the refractive index $n(x)$, grating period Λ and grating thickness d. The incident wave R_{in} enters the grating at $z = 0$ and couples inside the medium to the diffracted wave $S(z)$ under Bragg-matched conditions. At $z = d$ both waves exit the grating, with the diffracted beam propagating at the external Bragg angle Θ_B. (Own illustration based on [16, 19]).

A few simplifying assumptions form the basis of Kogelnik's theory. Firstly, it is assumed that the electric field is polarized perpendicular to incidence plane (s-polarization). Secondly, it is supposed that only two plane waves are propagating in the grating, which are the reference wave R (the transmitted beam, also referred to as the forward-diffracted wave) and the signal wave S (corresponding to the first-order diffracted beam) [19, 20].

Since only exact or near-Bragg incidence is considered and higher diffraction modes do not obey the Bragg condition, higher orders are negligible. Furthermore, the spatial modulation of the refractive index $n(x)$ is sinusoidal. Lastly, the coupled wave theory is only valid for thick gratings [19]. Thus, the grating couples the two waves, leading to an exchange of energy as they propagate within the grating. In the absence of absorption and higher diffraction orders, energy conservation implies that a decrease in the amplitude of the forward-diffracted wave is accompanied by a corresponding increase in the amplitude of the first-order diffracted wave [17, 19].

To better understand the underlying geometry consider Figure 2.2, which illustrates the schematic of a transmission volume grating, where the spatial modulation of the refractive index $n(x)$ varies sinusoidally [17, 19]. The grating is assumed to be one-dimensional, lossless and isotropic [20]. The unit vector $\hat{N}$ denotes the surface normal of the grating. The x-axis lies in the plane of incidence and is parallel to the boundaries of the recording medium, while the z-axis is oriented perpendicular to the surface of the medium. The grating vector $\vec{K}$ lies normal to the fringe planes and has a length of $|K| = 2\pi/\Lambda$. The thickness of the grating is indicated by d. At $z = 0$, the incident wave R_{in} enters the grating and, under Bragg-matched conditions, couples to the diffracted wave inside the medium. At the exit plane $z = d$, both waves $R(d)$ and $S(d)$ exit the grating, with the diffracted beam propagating at the external Bragg angle Θ_B [19]. Θ denotes the (external) angle of incidence and θ_B the Bragg angle, which is measured inside the medium (cf. Snell's law).

The propagation of both waves in the medium can be described by the scalar Helmholtz equation

$$\vec{\nabla}^2 E(x,z) + [n(x)k_0]^2 E(x,z) = 0, \tag{2.5}$$

with $k_0 = 2\pi/\lambda$ and $E(x,z)$ denoting the normalized amplitude of the electric field [17, 21]. The spatial variation of the refractive index can be expressed as

$$n(x) = n_0 + n_1 \cos(Kx), \tag{2.6}$$

where n_0 indicates the average refractive index and n_1 the refractive-index modulation [20]. The coupling between the two waves R and S is defined by the real-valued coupling constant

$$\kappa = \pi n_1/\lambda. \tag{2.7}$$

and describes the strength of energy interchange between R and S [15, 19]. The superposition of these two waves in the grating forms the total electric field E(x,z) with the wave amplitudes $R(z)$ and $S(z)$, which vary along the propagation direction as a result of the sinusoidal refractive-index modulation with

$$E(x,z) = R(z)\exp(i\vec{q}_R \cdot \vec{x}) + S(z)\exp(i\vec{q}_S \cdot \vec{x}), \tag{2.8}$$

where $\vec{q}_S$ represents the wave vector of the diffracted beam and $\vec{q}_R$ is the wave vector of the transmitted beam [19, 20]. They are related by the grating vector $\vec{K}$

$$\vec{q}_S = \vec{q}_R \pm \vec{K}. \tag{2.9}$$

It is important to mention, that this relation holds only under exact Bragg-matching conditions. In the case of off-Bragg, energy conservation is violated [20].

Violation of the Bragg condition $2\beta\sin(\theta_B) = K$ with the propagation constant $\beta = k_0 n_0$, due to angular deviations from the (internal) Bragg angle θ_B or wavelength deviations are described by the dephasing measure ϑ

$$\vartheta = K\left(\sin(\theta) - \frac{K}{2\beta}\right). \tag{2.10}$$

Substituting the total field (2.8) into the scalar Helmholtz-equation (2.5) yields two coupled differential equations for the wave amplitudes $R(z)$ and $S(z)$ [19, 20]. The second derivatives can be omitted, assuming that energy exchange between the two waves and also energy absorption happen slowly [17]. By solving the coupled-wave equations with transmission boundary conditions, the output amplitudes of the signal and reference waves can be obtained for volume phase gratings within Kogelnik's formulation, whereas Uchida's extension leads to modified coupled differential equations [19, 20].

Analytical comparisons by Sheridan in 1991 [21], later supported by independent experimental studies (see [20, 22]), revealed fundamental differences between the two first-order coupled-wave theories for transmission gratings in the off-Bragg regime. While Kogelnik's formulation, known as the K-vector closure method (KVCM), and Uchida's Beta-value method (BVM) predict identical diffraction efficiencies at exact Bragg incidence, their predictions differ significantly in the off-Bragg regime [21]. In particular, BVM provides an accurate description of the diffraction efficiency and the propagation direction of the diffracted beam under off-Bragg conditions, whereas KVCM exhibits limitations in this regime. The fundamental difference between the two approaches lies in how the diffracted wave-vector is defined and how energy conservation is treated. Kogelnik assumes that the wave-vector relation given in Eq. (2.9) remains valid also under off-Bragg conditions, although it is strictly valid only at exact Bragg incidence [15, 21]. This assumption leads to unequal magnitudes of the diffracted and transmitted wave vectors, $|\vec{q}_S| \neq |\vec{q}_R|$, thereby violating energy conservation. As a direct consequence, the phase at the exit surface is predicted incorrectly [20].

To resolve this inconsistency, Uchida formulates an alternative definition of the wave-vector of the diffracted $\vec{q}_S$ beam

$$\vec{q}_S = \vec{q}_R \pm \vec{K} + \Delta q_0 \hat{N} \tag{2.11}$$

and introduces the phase-mismatch parameter Δq_0

$$\Delta q_0 = \beta(c_R - c_S) \tag{2.12}$$

where $c_R = \cos\theta$ with the angle of incidence θ, and

$$c_S = \sqrt{\cos^2\theta + 2\vartheta/\beta} = c_R\sqrt{1 + 2\frac{\vartheta}{\beta c_R^2}}. \tag{2.13}$$

The parameter $\beta = k_0 n_0$ has a fixed magnitude, $\beta = |\vec{q_S}| = |\vec{q_R}|$, thereby ensuring energy conservation. Off-Bragg deviations are accounted for by the phase-mismatch parameter Δq_0, providing a geometrically consistent description of the off-Bragg case. This enables phase matching at the grating's exit interface, thus resulting in the correct prediction of the propagation direction of the diffracted beam [15, 20].

Considering a constant refractive index modulation n_1, solving the coupled-wave equations together with the wave-vector boundary condition of Eq. 2.11 yields the first-order diffraction efficiency

$$\eta_B = \frac{c_R}{c_S}\left[\nu_B \operatorname{sinc}\sqrt{\nu_B^2 + \xi_B^2}\right]^2, \tag{2.14}$$

with

$$\nu_B = \kappa\frac{d}{\sqrt{c_R c_S}} = \frac{n_1 \pi d}{\lambda\sqrt{c_R c_S}}, \tag{2.15}$$

$$\xi_B = \Delta q_0 \frac{d}{2} = \beta(c_R - c_S)\frac{d}{2}, \tag{2.16}$$

where, ν_B is the coupling strength and ξ_B is the off-Bragg parameter [20, 22].

In the case of an exponentially decaying refractive index modulation of the form $n_1(z) = n_1(0)\exp(-z/L)$, the coupled differential equations for the transmitted and first-order diffracted waves are transformed via differentiation and substitution into a second-order differential equation. This equation can then be identified as Bessel's differential equation. Applying appropriate boundary conditions for transmission gratings yields the general solutions for the amplitudes of the two coupled waves [11, 15]. For the complete formulation and derivation, see Ref. [11]. Within the framework of an exponentially decaying refractive index modulation, the depth-averaged value over the thickness d is given by

$$\bar{n}_1 = \frac{1}{d}\int_0^d n_1(z)\mathrm{d}z = n_1(0)\frac{L}{d}\left(1 - e^{-d/L}\right). \tag{2.17}$$

Here, L is the characteristic $1/e$ decay length describing the exponential decrease of the refractive index modulation along the z-direction. Uchida shows, that an attenuation of the refractive index modulation noticeably affects the diffraction efficiency and angular selectivity [11].

The Figure below shows the wave-vector diagram for off-Bragg conditions as described by the BVM approach.

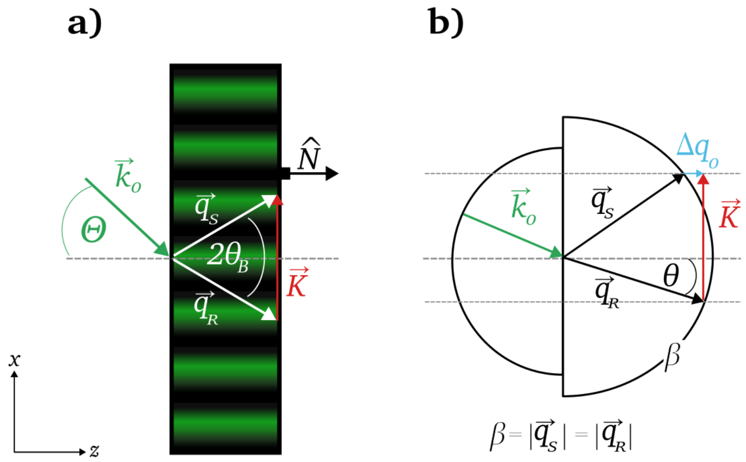

Figure 2.3.: a) Diffraction geometry of a transmission grating; b) Wave-vector diagram illustrating off-Bragg diffraction within the BVM framework. The BVM approach imposes $\beta = |\vec{q_S}| = |\vec{q_R}|$, ensuring energy conservation and geometrically consistent phase matching at the exit boundary. (Own schematic, adapted from [20]).

In summary, Uchida's approach provides a significant extension over Kogelnik's original theory. In contrast to Kogelnik's K-vector closure method, his Beta-value method provides a physically consistent description of off-Bragg diffraction by ensuring energy conservation and correct phase matching at the grating exit. The K-vector closure method reaches its limits for large angular detunings. By providing solutions for both a constant refractive index modulation n_1 and a depth-dependent, exponentially decaying refractive index modulation $n_1(z)$, Uchida establishes a comprehensive theoretical framework for the analysis of volume phase gratings. Consequently, his approach is strongly recommended for the analysis of experimental data, as emphasized by Fally (2023) [15]. Fitting the experimentally measured rocking curves within this theoretical framework enables the extraction of characteristic grating parameters, including the refractive index modulation n_1, the grating thickness d, the coupling strength ν and the decay length L.

2.3. LLL Neutron Interferometer

The LLL-interferometer enables interferometry with slow neutrons by employing three gratings in transmission Laue geometry, which act as beam splitters (BS) and mirrors to coherently split and recombine neutron beams [23]. It was originally developed for X-ray experiments and was later implemented for thermal neutrons with a wavelength of $\lambda = 2\text{Å}$ by Rauch et al. in 1974 [3], using a single, perfect crystal. To enable interferometry with very-cold neutrons, where wavelengths range from 5Å to 100Å, artificial diffraction gratings with a spacing larger than the neutron wavelength ($2\Lambda > \lambda$) are necessary [9, 23]. The geometry of the LLL interferometer for the VCN regime, as shown in Figure 2.4, is analogous to that of a Mach–Zehnder interferometer in light optics [2].

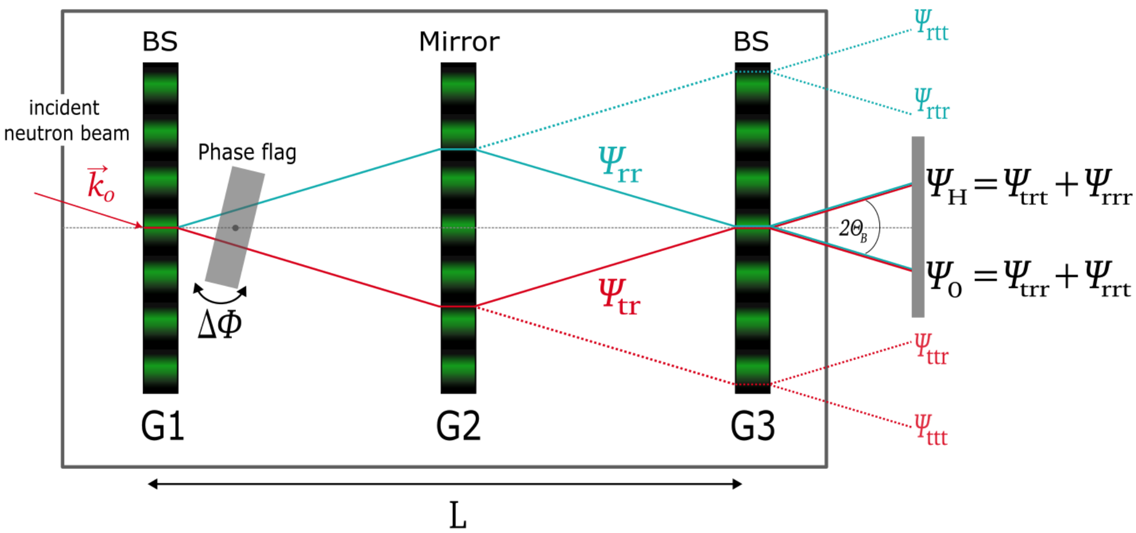

Figure 2.4.: Schematic of the LLL neutron interferometer. A collimated neutron beam is coherently split at grating G1, acting as a 50:50 beam splitter. Grating G2 acts as a Bragg mirror, redirecting the two partial beams towards grating G3, where they recombine and interfere. (Own schematic, adapted from [6]).

In neutron optics, the first (G1) and the third (G3) gratings ideally serve as 50:50 beam splitters, while the second (G2) grating operates as a mirror [6]. Any deviation results in a reduction of the contrast, in other words the visibility $v = (I_{max} - I_{min}) / (I_{max} + I_{min})$ of the interference pattern [1, 16]. The working principle of the LLL interferometer, according to [6], is as follows: A collimated neutron beam is incident on grating G1, where Bragg diffraction coherently splits it into two partial beams. At grating G2 the two beams are redirected towards grating G3, where they interfere and are diffracted into output beams, the 0-beam and the H-beam, which emerge separated by an angle of $2\Theta_B$. Rotating a phase flag introduces a controlled path difference between the two interferometer arms. While in the Mach–Zehnder interferometer a coherent laser beam is split into two separate beams and redirected by two mirrors toward a second beam splitter, where they interfere, in the LLL neutron interferometer the second grating simultaneously fulfills the role of both mirrors. The wave function Ψ_{tr} corresponds to the beam transmitted at G1 and reflected at G2, while Ψ_{rr} denotes the beam reflected at both G1 and G2. At grating G3, the amplitudes Ψ_{trr} and Ψ_{rrt} interfere to form the 0-beam, $\Psi_0 = \Psi_{trr} + \Psi_{rrt}$, whereas the amplitudes Ψ_{trt} and Ψ_{rrr} interfere to form the H-beam, $\Psi_H = \Psi_{trt} + \Psi_{rrr}$. Although several beam components emerge from grating G2, interference occurs only between those components that recombine into the same output direction at grating G3. The resulting interference intensities of the 0-beam and the H-beam depend on the relative phase $\Delta\Phi$ accumulated between the two paths, leading to counter oscillations [6].

The interferometer must meet specific criteria to enable high-precision interferometric measurements with very-cold neutrons and therefore the fabrication of adequate gratings, as well as their highly precise alignment are of crucial importance [6]. One significant criterion is the required diffraction efficiency that each grating must achieve. Since gratings G1 and G3 serve as 50:50 beam splitters, the diffraction efficiencies of the 0th and ±1st orders should satisfy $\eta_0 = \eta_{\pm 1} = 0.5$, while for the second grating G2 acting as a mirror, $\eta_{\pm 1} = 1$ is required. Furthermore, large diffraction angles are advantageous, as the interferometric sensitivity scales with the enclosed area between the beam paths. Since the diffraction angle increases with decreasing grating spacing Λ, short grating periods are beneficial. Lastly, the grating should exhibit low angular selectivity while maintaining high diffractive power, since VCN sources produce neutrons with a wide wavelength distribution [23]. Special materials are required to meet the conditions necessary for serving as holographic gratings in a VCN interferometer. One material that is particularly suitable as a neutron-optical element for high-precision interferometry is a nanodiamond–polymer composite, which represents a major innovation in the field of holographic grating fabrication [23, 24].

2.4. Nanodiamond-Polymer Composites (NDPC) for Holographic Gratings

Nanodiamond (ND) is a fascinating and promising carbon nanoparticle, characterised by a variety of excellent mechanical, thermal, electrical and optical properties, including a high hardness, low thermal expansion and a high refractive index [25]. For neutron optics the advantages of NDs lie in large coherent and negligible incoherent scattering, as well as low neutron absorption [24], making ND highly useful for the fabrication of ND-dispersed nanocomposite transmission holographic gratings for neutron optics [25].

The formation of holographic gratings in nanoparticle-polymer composites is based on photoinduced polymerization of a monomer in which nanodiamonds are uniformly dispersed [25]. When the material is illuminated with an interference pattern during holographic exposure, photoinitiators are activated in the bright regions, inducing polymerization there. Consequently, monomers diffuse from the dark to the bright regions, while photo-insensitive nanoparticles counterdiffuse toward the dark regions. This mutual diffusion continues until polymerization is complete, resulting in a periodic nanoparticle arrangement and the formation of a refractive index grating due to differences in composition and density [25, 26].

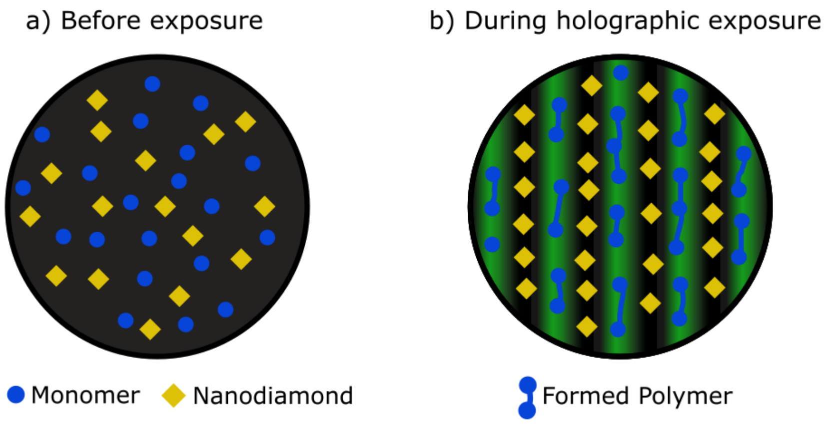

Figure 2.5.: Schematic illustration of the holographic grating formation in a NDPC. a) Homogeneous distribution of monomer molecules and nanodiamond particles before exposure. b) During holographic exposure, spatially modulated polymerization occurs due to the interference pattern, leading to the formation of a periodic volume grating. (Own schematic, based on [25])

These holographic nanodiamond-polymer composite (NDPC) gratings are highly effective at controlling light and also slow-neutron beams due to their large saturated refractive index modulation amplitudes at optical and also slow-neutron wavelengths [24, 25]. They are especially useful as beam splitters and mirrors in grating interferometers for cold and very cold neutrons [24]. For applications in slow-neutron optics, diffractive mirrors with high diffraction efficiency require a large refractive index modulation, moderate film thickness and short grating spacing [25]. Owing to these requirements, NDPCs are highly promising, as they exhibit high diffraction efficiencies at low angular selectivity and provide large diffraction angles, thereby acting as ideal optical elements for VCN interferometers [23].

Since artificial gratings based on neutron-photosensitive materials operate for both light and neutrons, the diffraction efficiency at exact Bragg incidence follows a structurally similar functional form. This similarity arises because, in both cases, the modulation is linked to periodic variations in material density. The recording process creates alternating ND-rich and ND-poor regions, which give rise to a modulation of polarizability and density for light and to a modulation of coherent scattering length and density for neutrons. For neutrons, the refractive index is defined as

$$n_N = 1 - \frac{\lambda^2}{2\pi} b_c \rho, \tag{2.18}$$

where b_c denotes the neutron–nuclear scattering length and ρ the number density [2]. Consequently, the first-order diffraction efficiency for neutrons at exact Bragg incidence is given by

$$\eta_{N|_{\theta=\theta_B}} = \sin^2\left(\frac{1}{2} d\lambda_N \Delta[b_c\rho]\right), \tag{2.19}$$

where $\Delta[b_c\rho]$ denotes the coherent scattering length density modulation [23]. For light, in accordance with Kogelnik's coupled-wave theory (see Ref. [19]), the corresponding expression reads

$$\eta_{L|_{\theta=\theta_B}} = \sin^2\left(\frac{n_1 \pi d}{\lambda_L \cos\theta_B}\right), \tag{2.20}$$

where the refractive index modulation n_1 arises from a periodic variation of the product of polarizability α and density ρ. Although both diffraction efficiencies share the same functional form, the optical refractive index modulation $n_1 \propto \Delta(\alpha\rho)$ and the neutron scattering length density modulation $\Delta(b_c\rho)$ originate from different microscopic interaction mechanisms. Therefore, no direct proportionality between the optical and neutron modulations can be assumed. Nevertheless, for the present NDPC material system, an empirical correlation between the optical refractive index modulation and the neutron scattering length density modulation has been observed in previous, yet unpublished studies (see Ref. [27]).

3. Experimental Setup and Methods

This chapter discusses the experimental procedure for realising the NDPC gratings, starting with the preparation of the photosensitive material and the fabrication of the samples, followed by the holographic recording process and subsequent optical characterization of the resulting gratings. In total three different gratings are required for realizing a VCN interferometer in LLL geometry as described in chapter 2.3. In order to serve as neutron-optical elements in a LLL interferometer and to fulfil the requirements for high-precision measurements, several conditions must be met by the gratings. First, a large-area grating (diameter $\approx 25\,\mathrm{mm}$) with homogeneous grating thickness d and laterally uniform refractive index modulation n_1 is required across the entire grating area. The first and third gratings (G1 and G3), which serve as beam splitters, have a target thickness of $d_0 = 25\,\mu\mathrm{m}$, while the central grating G2, functioning as a mirror, is intended to have a nominal thickness of $d_0 = 50\,\mu\mathrm{m}$. All three gratings must be fabricated reproducibly in successive holographic recordings. This ensures that highly parallel grating vectors $\vec{K}$ are defined during the recording process, ensuring precise mutual alignment in the interferometer and avoiding mismatches in grating orientation and diffraction properties that would reduce the interferometric visibility. Further, a grating period of $\Lambda \approx 500\,\mathrm{nm}$ is intended. For neutrons with a wavelength of $\lambda_N \approx 4.5\,\mathrm{nm}$, the corresponding Bragg angles yield a beam separation of 7.5 mm at the second grating in the LLL interferometer geometry. Such a beam separation is required to realize distinct interferometer paths without compromising alignment stability and beam overlap. Very importantly, the gratings should reach sufficiently high diffraction efficiency η and refractive index modulation n_1 for light. A target value of $n_{1,sat} \geq 0.01$ is considered, motivated by the relation between refractive index modulation, material contrast and nanoparticle redistribution reported in the literature (see Tomita et al. [25]). This value indicates the refractive index modulation necessary for achieving high diffraction efficiency in VCN using thick holographic gratings under the experimental conditions considered.

3.1. NDPC Material Preparation and Sample Fabrication

3.1.1. Preparation of NDPC Material

The preparation of holographic NDPC gratings starts with the proper mixing of the relevant chemicals together with the NDs. The chemicals used for this procedure are ethoxylated dipentaerythritol hexaacrylate (A-DPH-12E, Shin-Nakamura Chem. Co. Ltd., purity $\geq$ 99.0%), acrylic acid tetrahydrofurfuryl ester (THF-A, Tokyo Chemical Industry Co. Ltd., purity $>$ 98-0%), Rose Bengal (RB, Tokyo Chemical Industry Co.

Ltd.), N-Phenyl glycine (NPG, Sigma-Aldrich, purity 97%) and ND-suspension sol (Daicel Corporation, ND-concentration 3.1 wt%), which is a mixture of monodispersed NDs and methyl isobutyl ketone (MIBK). RB together with NPG serves as the photoinitiator system for the polymerization process, which is sensitive to green light, where the maximum absorbance is at 565 nm, and insensitive to red light (see Ref. [27]).

Figure 3.1.: Chemicals used for the preparation of the NDPC material.

The following table lists the target amount of each chemical required to obtain the ideal mixture for the preparation of NDPC samples, based on values determined in previous, yet unpublished studies (see Ref. [27]).

Component	Target weight [mg]
A-DPH	160.0
T-HFA	326.6
ND-sol	3163.0
RB	4.5
NPG	9.0

Table 3.1.: Optimal values for the weight [mg] of ADP-H, THF-A, ND-sol, RB and NPG in order to obtain the ideal NDPC syrup.

The first step in material preparation is the mixing of the chemicals, which is done in a dark laboratory with only red light, as the photoinitiator system is insensitive to the red. The mass of each component is precisely measured using an analytical balance (Mettler Toledo ME Analytical Balance, readability 0.1 mg) and transferred into a glass vial together with a magnetic stirring bar. A vortex mixer is then used to properly mix all chemicals and obtain a homogeneous syrup. The next step involves the evaporation process of the MIBK portion. The mixed syrup in the vial is placed in a vacuum chamber and heated on a hot plate at approximately 50°C under magnetic stirring, as shown in Fig. 3.2. During this process, the MIBK evaporates and leaves the NDs in the syrup, which gradually becomes highly viscous. The magnetic stirring bar ensures continuous mixing and homogeneous dispersion of the NDs during the evaporation process, with the hotplate providing a rotational speed of 200 rpm. The final viscosity is highly sensitive to the accurately measured weights of the chemical components as well as to the evaporation time. An evaporation time between 2-6 hours is required. Deviations of approx. ±20–30 minutes can lead to a degradation of the material quality, for example the formation of agglomerates. It should be noted that the required evaporation time increased from approx. two hours in earlier preparations to up to about six hours in later attempts, for reasons that remain unclear. In total, after several preparation attempts, two different NDPC syrup batches, denoted S13 and S14, were prepared for the final gratings. An overview of the measured masses of the chemical components used in these samples is given in Table A.1 and A.2 in the Appendix.

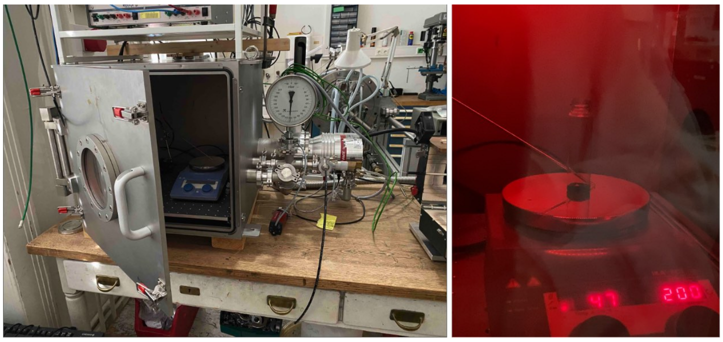

Figure 3.2.: Photograph of the vacuum chamber showing the NDPC material in a vial placed inside the chamber on a hot plate. Equipment and facilities kindly provided by Dr. Puchegger, Fakultätszentrum für Nanostrukturforschung.

3.1.2. Fabrication of NDPC Samples

After the successful evaporation of MIBK and the resulting formation of the desired syrup-like consistency, the individual samples are prepared for use as holographic NDPC gratings. Once again, a dark laboratory is used, with only a red light present, to avoid any premature exposure of the NDPC material. The required mechanical components for each sample, shown in Fig. 3.3, and the detailed fabrication procedure for sample batch S14 are described below and illustrated in Fig. 3.4. Note that an alternative fabrication procedure was used for sample series S13. This procedure proved to be less reliable and is therefore described only for completeness in Appendix A.2.

Each sample requires two circular plane-parallel Suprasil glass substrates (Präzisions Glas & Optik GmbH, UV-grade fused silica with >80% transmission at 185 nm) with a thickness of (3 ± 0.025) mm and a diameter of (65 ± 0.25) mm. For each sample, three spacers made of brass are used to control the grating thickness. The spacers are cut into rectangular pieces (approxim. 10×5 mm), bent into a U-shape and placed at equal distances around the outer edge of the first glass substrate. This substrate is then placed into a sample holder, which serves as the grating mount used later during holographic recording. Subsequent to that, five to six small drops of the NDPC syrup are dropped in the center of the first glass. Then, the second substrate is placed on top of the material and pressed down until a homogeneous, circular layer is formed. The NDPC material between the two glass substrates must be distributed evenly and have a constant thickness within a circular area of approxim. 25 mm in diameter, since the subsequent holographic recording forms a circular grating of the same size. The thickness of this layer is defined by the brass spacers, corresponding to 50 μm (for G2) and 25 μm (for G1 and G3).

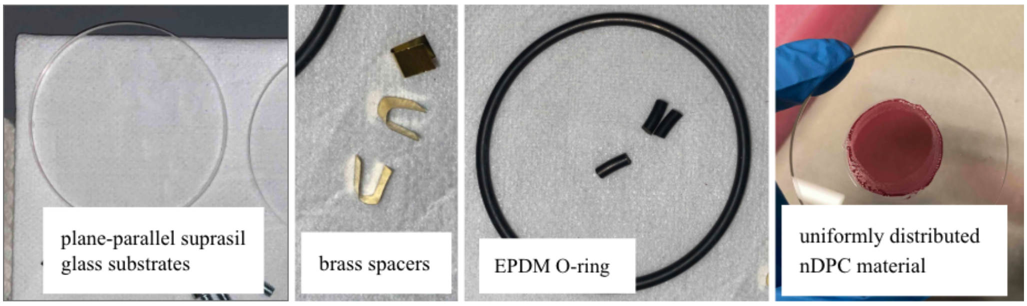

Figure 3.3.: Mechanical components required for sample fabrication.

Following this, three pieces of EPDM (approxim. 3×7 mm), cut from O-rings (Angst + Pfister AG, Normatec Compound EPDM 70.00-02, inner diameter 59.36 mm, cross-section 3.00 mm), are placed directly above the three-contact points of the brass spacers on the upper glass substrate, acting as compliant buffers. The clamping ring of the sample holder is then set in place to secure the sample assembly. Using a torque wrench (PROXXON MC 2, scale: 0.4 Nm to 2.0 Nm), three screws of the clamping ring are tightened to a defined torque of 0.4 Nm. This configuration forms a uniform three-point support that is precisely aligned with the underlying three-point support of the spacers. Such precise three-point fixation ensures that no mechanical stress or warping of the glass substrates occurs, keeping them completely planar and thereby enabling the required formation of a large-area, homogeneous thin film with consistent thickness.

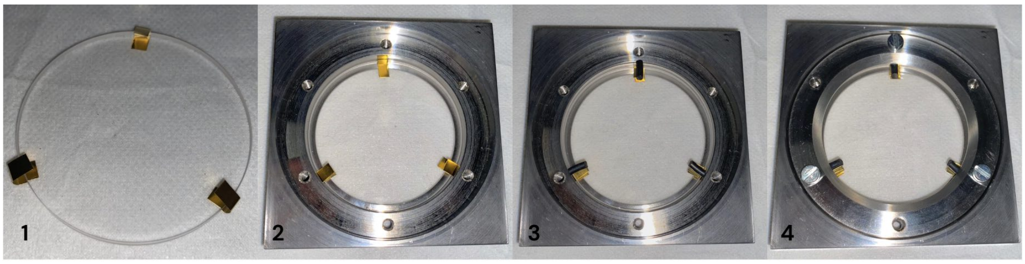

Figure 3.4.: Step-by-step demonstration of the sample assembly (S14), shown without the NDPC syrup: 1. The three brass spacers are placed on the first glass substrate. 2. The substrate is inserted into the sample holder base. 3. After the (hypothetical) addition of the syrup and the second substrate, the three EPDM buffers are placed on top, aligned with the spacers. 4. The clamping ring is placed and fastened, securing the full assembly.

The assembled samples are then heated in an oven at 80°C for 30 minutes and cooled to room temperature afterwards. After that, each sample holder is screwed centrally onto a sample mounting block, which secures the holder and the enclosed sample in position. While two samples are mounted on a super-planar aluminum plate with dimensions of $150 \times 150 \times 40$ mm (Johann Fischer Aschaffenburg, Präzisionswerk GmbH Co. KG.), one sample is mounted onto a high-precision 6-axis piezoelectric stage (PI, Physik Instrumente, Model P-562.6CD, Controller System E-712). The dimensions of this stage are compatible with the aluminum mounting plates. The purpose of these blocks is to serve as stable grating mounts with identical dimensions, ensuring consistent alignment and reproducible positioning of all samples during the recording process. It simultaneously guarantees the geometric consistency required for their arrangement in the VCN interferometer later. Regards the PI stage, it enables motion in six degrees of freedom. For the linear axes (x, y, z), the PI has a travel range of 200 μm and a resolution in the sub-nanometer range. For the rotational axes (θ_x, θ_y, θ_z), the PI provides a tilt range of 1000 μrad and an angular resolution of 0.1 μrad [28]. This level of precision is essential for accurate phase shifting and fine alignment within the VCN interferometer later.

The samples, now fully assembled, are then prepared for subsequent holographic recording. Each sample is recorded individually in a separate, sequential holographic recording. The following image shows examples of the fully assembled grating mount (shown here for illustrative purposes only, without NDPC syrup).

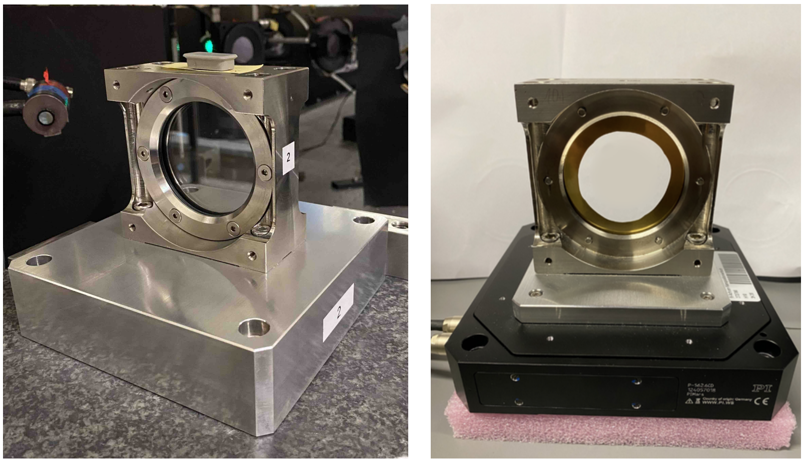

Figure 3.5.: Examples of the fully assembled grating mounts (shown without NDPC material) prepared for the holographic recording process: *Left panel*: Aluminum block. *Right panel:* 6-axis piezoelectric nanopositioning stage.

3.2. Holographic Recording of the NDPC Gratings

After completion of the sample preparation, holographic recording of the gratings in the photosensitive NDPC material is carried out. The goal is to obtain three identical volume gratings in a sequence of identical holographic exposures under exactly the same conditions. This requires a holographic recording setup capable of accurately reproducing the same grating properties in each recording. Therefore, highly precise alignment of the samples is required during the writing process.

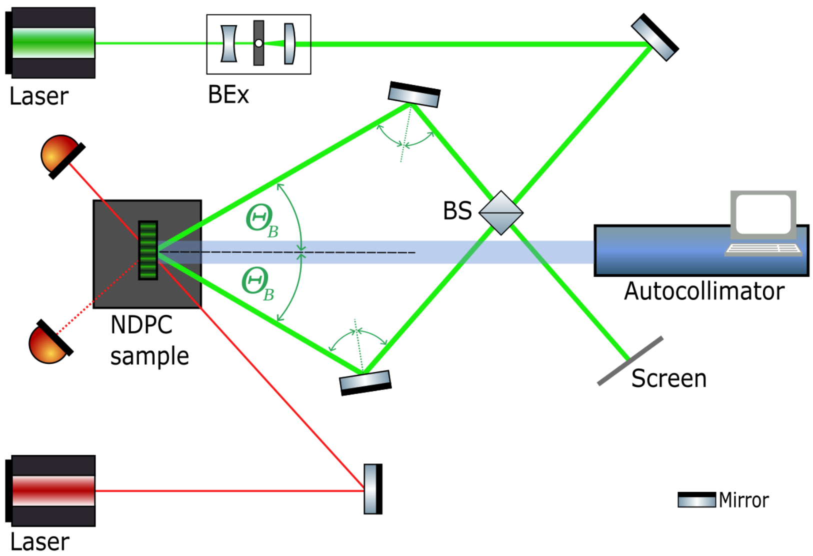

Figure 3.6.: Schematic of the holographic two-wave mixing setup used for recording the NDPC volume gratings. The green laser beams interfere at the sample position at an angle of $2\Theta_B = 60.08°$. An autocollimator defines the optical reference axis and is used for precise adjustment of yaw and pitch angle, ensuring that all subsequent gratings are aligned identically to the first recorded grating with respect to the recording beams.

The entire procedure is carried out in a dark optical laboratory, using only a red light source. To generate holographic volume gratings, a two-wave mixing setup with s-polarized light is employed, in accordance with the schematic representation shown in Fig. 3.6. The setup utilizes a coherent laser source operating in the green light at a wavelength of 514 nm (Coherent Genesis MX SLM Series, Optically Pumped Semiconductor Laser (OPSL)). A Beam Expander System (BEx), consisting of a 10×-objective, a 50 μm pinhole and a 200 mm collimating lens, is used to expand the incident laser beam to a diameter of 27 mm. The expanded beam is then split into two separate writing beams by a beam splitter (BS). These two coherent beams are directed to the sample via mirrors and interfere at a specific recording angle Θ_B, the external Bragg angle, where they illuminate the sample symmetrically. Each beam is incident at an recording angle of $\Theta_B = 30.54°$ with respect to the surface normal, resulting in an intersection angle of $2\Theta_B = 61.08°$ between the two writing beams. The final grating period Λ is defined by the angle Θ_B, according to the Bragg condition (see Eq. (2.4)). The core requirement of this arrangement is the precise alignment of the grating vector. It is crucial that the grating vector is exactly parallel for each grating and normal to the glass substrate surface. The correct overlap of the two writing beams is verified by observing a stable interference pattern of the back-reflected beams on a screen. The precise superposition of the beams at the designated plane of the NDPC sample ensures the formation of a well-defined interference pattern, thereby enabling the photoinduced formation of the grating.

To ensure the fabrication of three identical gratings with highly parallel grating vectors, precise and reproducible alignment during the recording process is required. This is achieved by using a super-planar granite bench (Johann Fischer Aschaffenburg, Präzisionswerk GmbH Co. KG) with dimensions of $300 \times 300\ \text{mm}^2$. The aluminum mounting blocks (or the PI stage) carrying the samples are placed sequentially on the granite bench during holographic exposure, ensuring a well-defined and planar grating mounting. The high planarity of the granite surface minimizes deviations in pitch and roll angles during the recording process. The granite bench used for holographic recording is a scaled-down version of the granite bench employed in the LLL interferometer setup at the ILL, as shown in Fig. 3.7. Using this geometrically consistent reference surface ensures that the fabricated gratings can later be positioned reproducibly in the VCN interferometer and that they are mutually consistent with respect to grating vector orientation and surface planarity, which is essential for neutron interferometry.

Figure 3.7.: Left panel: photograph of the granite bench used for the LLL interferometer setup (Image taken from Johann Fischer Aschaffenburg). Right panel: photograph of the small granite bench used for the recording of the gratings.

The angular alignment of the gratings in yaw, pitch and roll is highly critical and sensitive. In particular, the roll angle must be adjusted with the highest possible precision, as the maximum permissible deviation is only a few microradians, which is ensured by the use of the super-planar granite bench. In addition, an electronic autocollimator (TriAngle

Electronic Autocollimator, Model TA 1000-115, TRiOPTICS GmbH) is employed for the precise adjustment and monitoring of the yaw and pitch angles of the grating surfaces with microradian accuracy. The autocollimator measures small angular tilts by detecting the displacement of a reflected light beam relative to a reference axis, using an internally generated low-intensity, collimated light beam reflected from the grating surface. Prior to the actual holographic recording of the final gratings, the bisector of the two recording beams is determined experimentally. For this purpose, a test mirror is placed at the exact position where the samples will later be mounted. The optical setup, including the beam splitter and steering mirrors, is carefully adjusted until the retroreflected writing beams overlap and generate a symmetric and stable interference pattern on a distant screen. The appearance of a symmetric interference pattern confirms that the two recording beams are arranged symmetrically and that their bisector is well defined. This bisector serves as the fundamental optical reference axis of the setup. Since the grating vector is oriented perpendicular to the bisector of the two recording beams, aligning the surface normal of the sample with the bisector ensures a well-defined and reproducible grating vector orientation. The bisector direction therefore defines the zero yaw position for all samples. Subsequently, the optical axis of the autocollimator is aligned to coincide with this bisector direction. From this point onward, the zero position of the autocollimator corresponds to the defined optical reference axis. This procedure ensures that all gratings are mutually aligned with parallel surface normals and, consequently, parallel grating vectors with respect to pitch and yaw. In particular, once the first grating has been recorded, the autocollimator guarantees that the relative orientation of each subsequent grating with respect to the writing beams, and thus the resulting grating vector, is identical to that of the first recorded grating. The defined optical reference axis is later used to reproducibly position the gratings on the granite bench in the LLL interferometer setup.

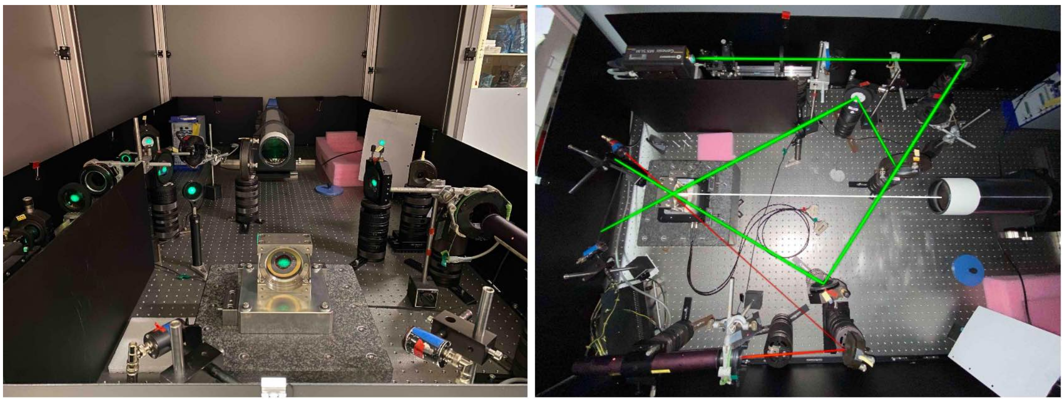

Figure 3.8.: Photographs of the holographic recording setup for the NDPC gratings, showing the symmetric two-beam geometry. The laser beam paths and the optical axis are indicated schematically for clarity.

Figure 3.8 shows a photograph of the experimental arrangement, with the laser beam paths and the optical axis, defined by the autocollimator and corresponding to the bisector of the two writing beams, indicated schematically for clarity.

The measured angular deviations are displayed by the control software (OptiAngle 6), as shown in Fig. 3.9, as angular components in the horizontal (X, yaw) and vertical (Y, pitch) directions. The autocollimator provides sub-microradian sensitivity, with an angular resolution of 0.01 arcsec ($\approx 0.05\,\mu$rad) and an accuracy of 0.2 arcsec ($\approx 1\,\mu$rad), and operates over a measurement range of $\pm 1500\,\mu$rad for yaw and pitch. The camera image shows a central reference cross, defining the reference axis, together with reflected signal crosses originating from different optical surfaces of the glass substrate (Merkmale), such as the front and back surfaces. Deviations of the reflected signal positions relative to the reference cross indicate an angular tilt of the reflecting surface in yaw or pitch. Rotations about the surface normal (roll angle) and pure translations of the grating do not affect the measured angles within the valid detection range of the autocollimator.

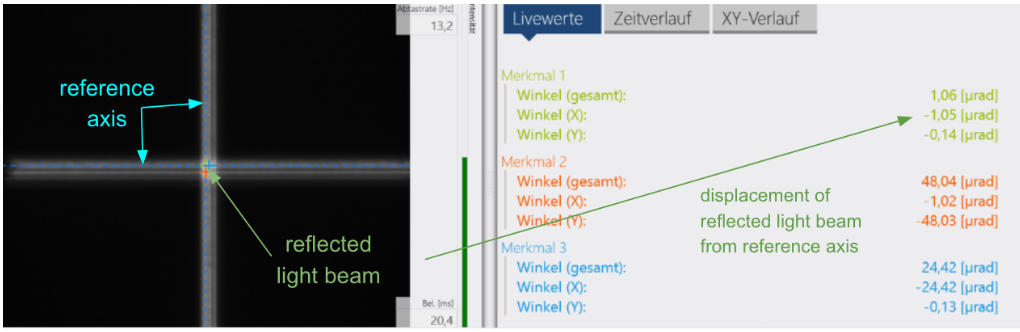

Figure 3.9.: Autocollimator control software interface (OptiAngle 6) showing the angular deviation of the reflected beam from the reference axis.

Once the bisector of the recording beams has been correctly established and the autocollimator has been aligned with this optical reference axis, the experimental procedure can begin. The first sample is mounted on the small granite bench and its surface normal is aligned with the defined zero yaw position by adjusting the yaw and pitch angles according to the angular readout provided by the autocollimator software. After the alignment has been completed, the holographic recording of the first sample can be started. The expanded green laser beam exposes the NDPC material at an intensity of $200\,\mathrm{mW/cm^2}$ for a duration of 1800 s, thereby recording the volume grating. Following the successful writing of the first holographic grating, the second and third samples are mounted one after another on the granite bench and adjusted consistently using the autocollimation system as the established reference. For sample G3, the piezoelectric stage is additionally used to correctly adjust the angles by employing its different rotational axes. During recording, a red HeNe laser operating at 632.8 nm (Melles Griot 05-LHP Series, Helium-Neon) is used simultaneously to monitor the temporal buildup of the grating, as the

NDPC material is insensitive at this wavelength. The laser is aligned at the Bragg angle corresponding to the red wavelength such that it probes the center of the forming grating. In this configuration, the diffracted intensity of the red beam provides a direct measure of the diffraction efficiency during the grating formation process, which is monitored by photodiodes positioned in the zeroth and first diffraction orders.

Consequently, this recording procedure resulted in three NDPC holographic volume gratings: G1 (aluminium plate mount, nominal thickness $d_0 = 25\,\mu$m), G2 (aluminium plate mount, $d_0 = 50\,\mu$m) and G3 (PI stage mount, $d_0 = 25\,\mu$m). The complete VCN interferometer at the neutron facility requires then the three holographic volume gratings to be mounted on the extremely planar granite bench, which ensures mechanical stability (Johann Fischer Aschaffenburg, Präzisionswerk GmbH Co. KG, with dimensions of $300 \times 1760\,\text{mm}^2$). The gratings must be positioned equidistantly from each other and require highly precise mutual alignment, achieved using again the autocollimator. The total specified length of the interferometer is $L = 1.5\,$m.

3.3. Optical Readout Setup for Rocking Curve Measurements

After the successful recording of holographic NDPC volume gratings, optical readout is performed to measure rocking curves, which describe the diffraction efficiency $\eta(\Theta)$ as a function of the external angle of incidence Θ. From these measurements, the grating parameters are extracted. The diffraction efficiency η is directly obtained, while the effective grating thickness d, grating period Λ, refractive index modulation n_1, decay length L and coupling strength ν are determined by fitting the rocking curves. The analysis is based on the coupled-wave theory following the model of Uchida introduced in chapter 2.2.

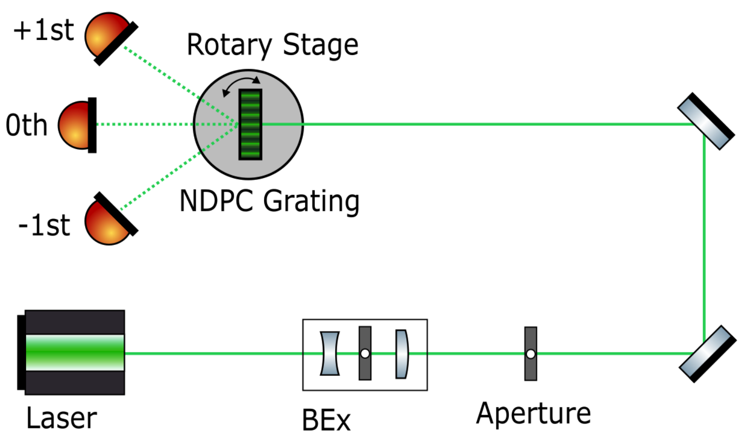

Figure 3.10.: Schematic of the optical readout setup for rocking curve measurements. A green laser at 543.5 nm illuminates the sample, while three photodiodes record the zeroth-order and ±1st diffraction orders.

The optical readout setup, shown in Fig. 3.11, consists of a green laser (Coherent, HeNe) operating at a wavelength of 543.5 nm. The laser beam is expanded and spatially filtered using a beam expander system (BEx) and an aperture in order to obtain a collimated, planar wavefront. The beam is then guided by two mirrors and directed onto the sample. The NDPC grating is mounted on a motorized rotation stage, allowing controlled angular scanning around the Bragg angles of the ±1st diffraction orders for rocking curve measurements. When the incident beam fulfills the Bragg condition, diffraction into the ±1st orders occurs, reaching maximum intensity at incidence angles of ±32.5° for the readout wavelength of 543.5 nm. Behind the sample, three photodiodes are positioned to detect the transmitted zeroth-order beam as well as the diffracted -1st and +1st orders. Fig. 3.11 shows photographs of the optical readout setup taken from above and a close-up demonstrating how the incident readout beam is aligned to probe the center of the grating during the readout measurement.

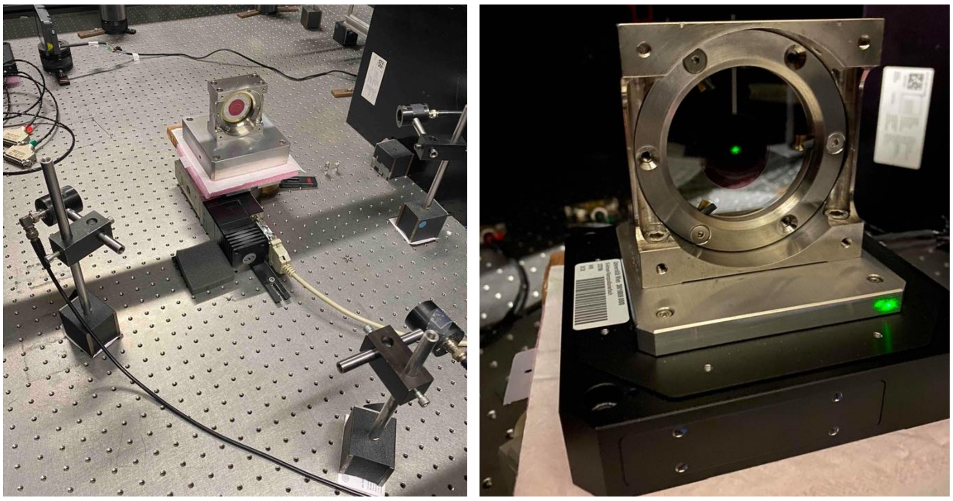

Figure 3.11.: Photograph of NDPC grating, mounted on a motorized rotation stage for angular diffraction measurements. *Left panel*: Top view of the setup showing the arrangement of the photodiodes for detection of the -1st, 0th and +1st diffraction orders. *Right panel*: Close-up showing the incident readout beam probing the center of the grating

Before optical readout, the recorded gratings are subjected to a post-curing step by illumination with a broadband LED source (30 W). The samples are exposed for different durations (Grating G1: 40 h, Grating G2: 15 h, Grating G3: 90 h) to ensure sufficient post-curing prior to readout. The exposure durations were chosen empirically and are not the result of a systematic optimization. Post-curing is performed to complete the polymerization process and to stabilize the refractive index modulation of the recorded gratings, which may slightly increase during this step. Subsequently, rocking curve measurements are performed for each grating.

3.4. Fabrication of Additional Gratings

Following the assembly of the interferometer using gratings G1, G2 and G3, it became evident that the wavelength distribution of the VCN beamline was narrower than initially assumed during their fabrication ($\lambda_N \approx 4.5\,\text{nm}$) and that further improvements to the interferometer setup and grating parameters were possible. This motivated a subsequent fabrication run to produce additional gratings with modified thickness parameters for the VCN interferometer.

For this purpose, a new NDPC material batch S15 was prepared. Table A.3 in the Appendix provides an overview of the measured masses of the chemical components used in sample set S15. From this material, four gratings were fabricated (referred to as C-PI, C-1, C-2 and C-3), three intended for use in the LLL interferometer and one additional grating as a spare. All gratings had a target thickness of $50\,\mu$m. Consequently, the target thickness for the first and last gratings acting as beam splitters in the LLL interferometer was adjusted from $25\,\mu$m to $50\,\mu$m. For these gratings, newly designed sample holders were employed. The clamping rings were manufactured with three raised contact points on the inner circumference, forming a defined three point support for the sample, as shown in the following figure.

Figure 3.12.: Modified clamping ring used for sample set S15, incorporating three raised contact points for defined three point support (highlighted in green).

This design preserved the three point support concept previously used for sample set S14 while eliminating the need for an additional EPDM O-ring as a compliant buffer. The remaining preparation steps for the samples were carried out following the same procedure as in the previous run S14. One sample was mounted on the piezoelectric stage (C-PI), while the other three samples were mounted on the aluminum plates (C-1, C-2 and C-3). Subsequent exposure to the interference pattern resulted in four additional gratings. The latter enabled further light-optical characterization and the subsequent realization of the LLL interferometer setup, consistent with the approach used for the previously fabricated gratings.

4. Experimental Results

This section presents the experimental results of the fabrication of the NDPC gratings, the holographic recording process and the subsequent optical readout. The results include the temporal buildup of grating formation during holographic recording, the corresponding evolution of the refractive index modulation and the measured rocking curves of the three final gratings. All relevant grating parameters are extracted and summarized. Also presented are the characterisation results of the additional fabricated gratings.

4.1. Fabrication Outcome of the NDPC Gratings

In the course of the experimental work, two different NDPC syrups, S13 and S14, were prepared, from which several samples were produced. Three of these samples were successfully fabricated into the gratings G1, G2 and G3. The use of two sample sets was a consequence of the preparation method. For sample set S13, the procedure followed a method that had been effective in previous fabrications. This initial fabrication protocol is detailed in Appendix A.2. In this case, however, the method failed for most samples and only one sample could later be used to produce a grating, namely grating G3. For the remaining samples of this set, the material deformed unevenly between the glass substrates, leading to an irregular structure, as shown in the image A.2. The procedure for sample set S14, described in chapter 3.1.2, was used for gratings G1 and G2. The appendix A.1 provides the measured masses of all components for both sample sets.

The following table summarizes the fabricated gratings, including the sample preparation method (indicated by the corresponding sample set S13 or S14), the spacer thickness used to define the target grating thickness d_0, the mounting used, the laser intensity I, the recording duration t_R and the post-curing duration t_P.

Grating	Sample set	Spacer thickness d_0	Mounting type	Laser intensity I	Recording time t_R	Post-curing time t_P
G1	S14	$25\,\mu$m	PI stage	$200\,\text{mW/cm}^2$	1800 s	40 h
G2	S14	$50\,\mu$m	Alumin. block	$200\,\text{mW/cm}^2$	1800 s	15 h
G3	S13	$25\,\mu$m	Alumin. block	$200\,\text{mW/cm}^2$	1800 s	90 h

Table 4.1.: Overview of the fabricated NDPC gratings and their fabrication parameters.

The temporal buildup dynamics of the NDPC gratings G1, G2 and G3 during holographic recording, monitored by the red laser (632.8 nm), is shown in the following figures. For each NDPC grating, the recording time is 1800 s. The upper panel of each figure shows the time evolution of the transmitted zeroth-order intensity, the first-order diffracted intensity, together with their sum. The lower panel shows the corresponding time evolution of the calculated diffraction efficiency. The recorded signal corresponds to the photocurrent of the photodiode, which is proportional to the optical intensity.

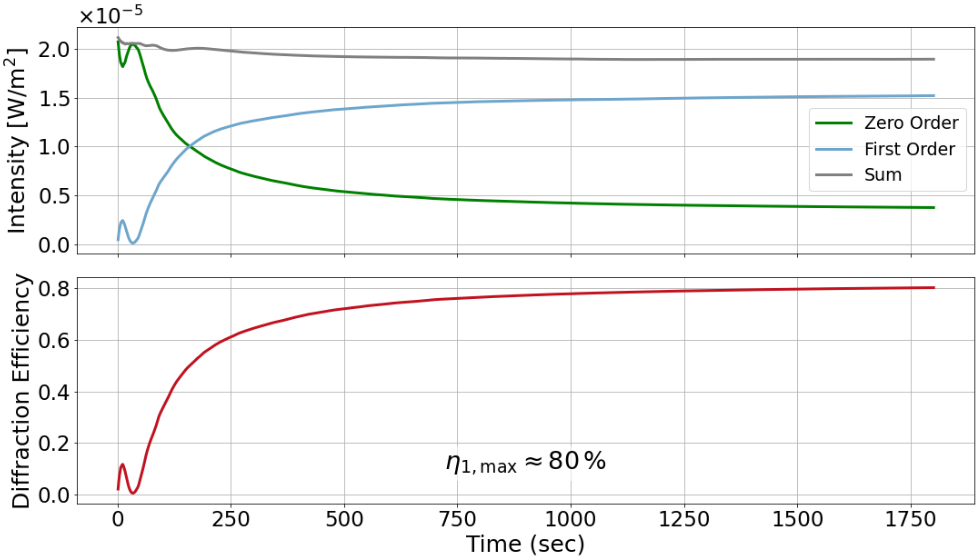

Figure 4.1.: Temporal grating buildup dynamics during holographic recording for G1 over 1800 s. *Top panel*: Time evolution of zeroth- and first-order intensities and their sum. *Bottom panel*: Time evolution of calculated diffraction efficiency.

Using a wavelength of 632.8 nm, a maximum diffraction efficiency of approx. 80% is obtained for grating G1 (Fig. 4.1). For grating G2 (Fig. 4.2), the maximum diffraction efficiency reaches approx. 89% and for grating G3 (Fig. 4.3) it reaches 82%. The total intensity, given by the sum of the zeroth-order and first-order intensities, remains approximately constant during the recording process for all gratings, which is important to demonstrate that no significant intensity losses occur during the optical readout. During the first approximately 50 s of the recording process, a pronounced transient behavior is observed. The first-order diffracted intensity initially increases rapidly while the zeroth-order intensity decreases correspondingly. This behavior is followed by a temporary reduction of the first-order intensity to nearly zero. As a result, the diffraction efficiency exhibits an initial increase followed by a decrease during this early stage. After the transient regime, the diffraction efficiency increases again and evolves more slowly towards saturation. Gratings G1 and G3 exhibit a monotonic, saturating increase of the diffraction efficiency, whereas grating G2 shows a slight decrease after reaching its maximum efficiency.

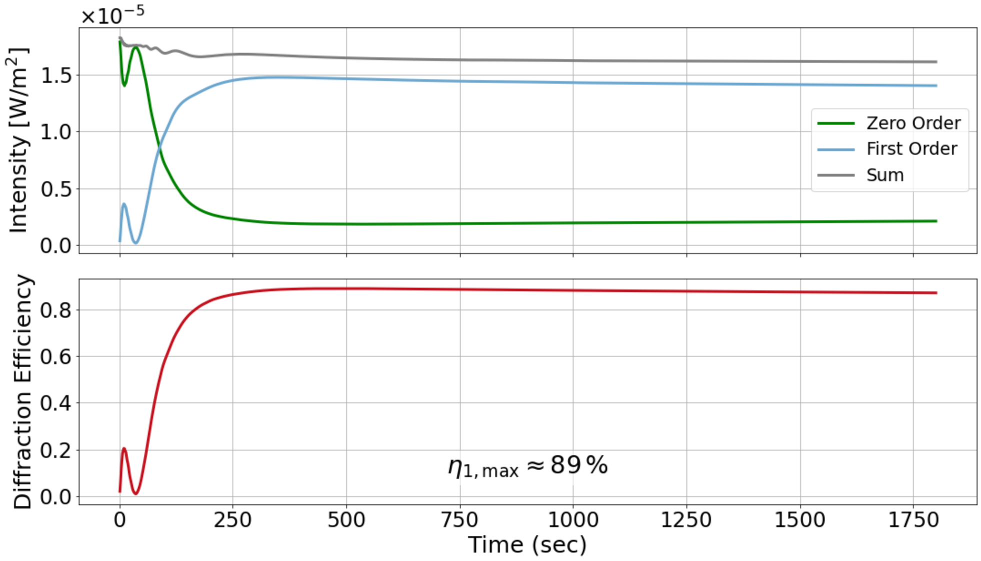

Figure 4.2.: Temporal grating buildup dynamics during holographic recording for G2 over 1800 s. *Top panel*: Time evolution of zeroth- and first-order intensities and their sum. *Bottom panel*: Time evolution of calculated diffraction efficiency.

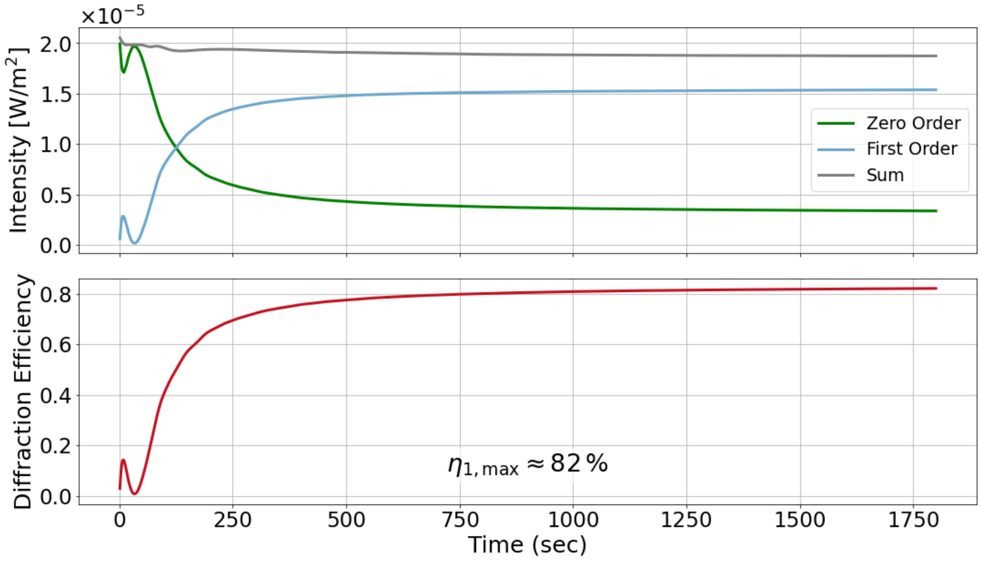

Figure 4.3.: Temporal grating buildup dynamics during holographic recording for G3 over 1800 s. *Top panel*: Time evolution of zeroth- and first-order intensities and their sum. *Bottom panel*: Time evolution of calculated diffraction efficiency.

As explained before, an autocollimator was used to monitor the angular alignment of the gratings during their installation on the granite bench as well as during holographic recording. In order to quantify possible changes in yaw and pitch angles, autocollimator readings were taken for each grating before and after recording. Possible sources of angular changes include mechanical mounting effects, such as excessively tightened screws, as well as thermally induced deformations of the glass substrates caused by laser-induced heating. For each grating, multiple reflection signals ("Merkmal 1–3") are detected, originating from different surfaces of the glass substrate. Merkmal 1 corresponds to the reflection signal with the highest measured intensity and originates from the front surface of the glass substrate, which therefore serves as the reference surface for the measurements. The following figures present the autocollimator readout for gratings G1, G2 and G3. The upper panels show the angular alignment prior to holographic recording, while the lower panels show the readout after recording of the final fabricated gratings. For grating G1 (see Fig. 4.4), an analysis of Merkmal 1 shows that the yaw angle (X) changed by approxim. 36 μrad and the pitch angle (Y) by about 17 μrad during the recording process. For grating G2 (see Fig. 4.5), changes of about 5 μrad in yaw and 11 μrad in pitch were observed, while for grating G3 (see Fig. 4.6) the corresponding changes were approxim. 7 μrad in yaw and 9 μrad in pitch. The total angular deviation ("Winkel gesamt"), obtained from the combined changes in yaw and pitch, is approxim. 40 μrad for grating G1, 12 μrad for grating G2, and 10 μrad for grating G3. This indicates that all gratings exhibited only small angular changes during recording, with grating G1 showing the largest deviation.

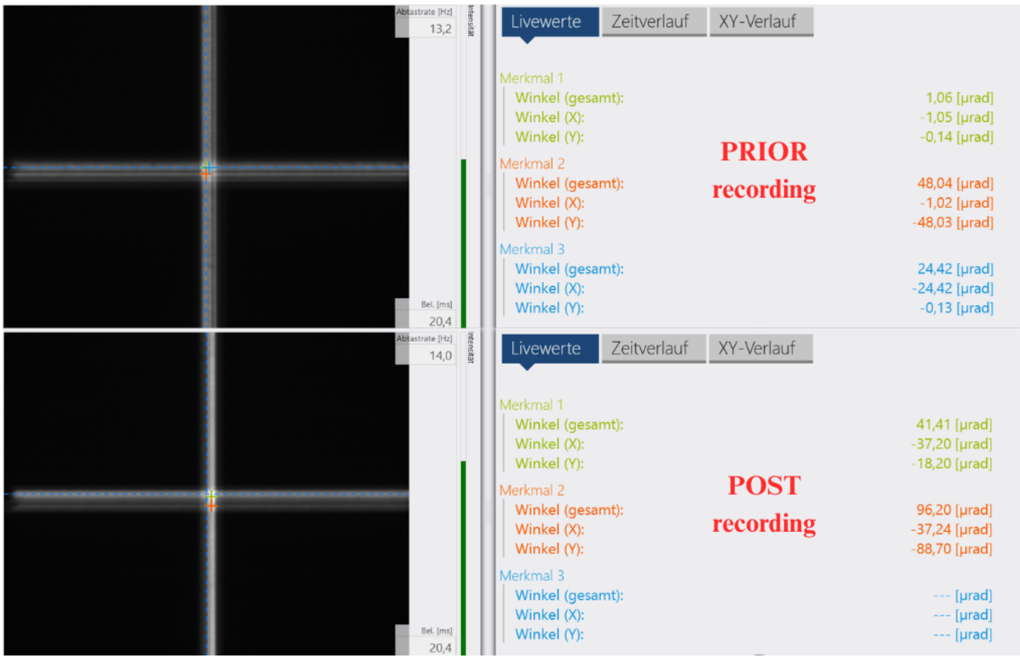

Figure 4.4.: Autocollimator readout of the angular alignment of grating G1. *Top panel*: Before holographic recording. *Bottom panel*: After holographic recording.

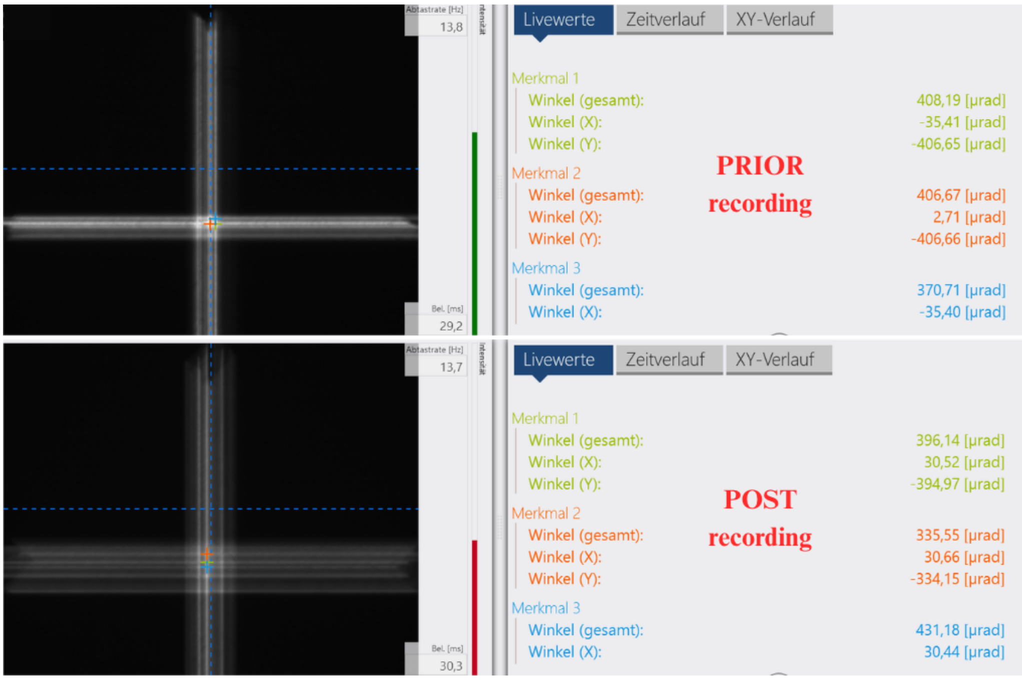

Figure 4.5.: Autocollimator readout of the angular alignment of grating G2. *Top panel*: Before holographic recording. *Bottom panel*: After holographic recording.

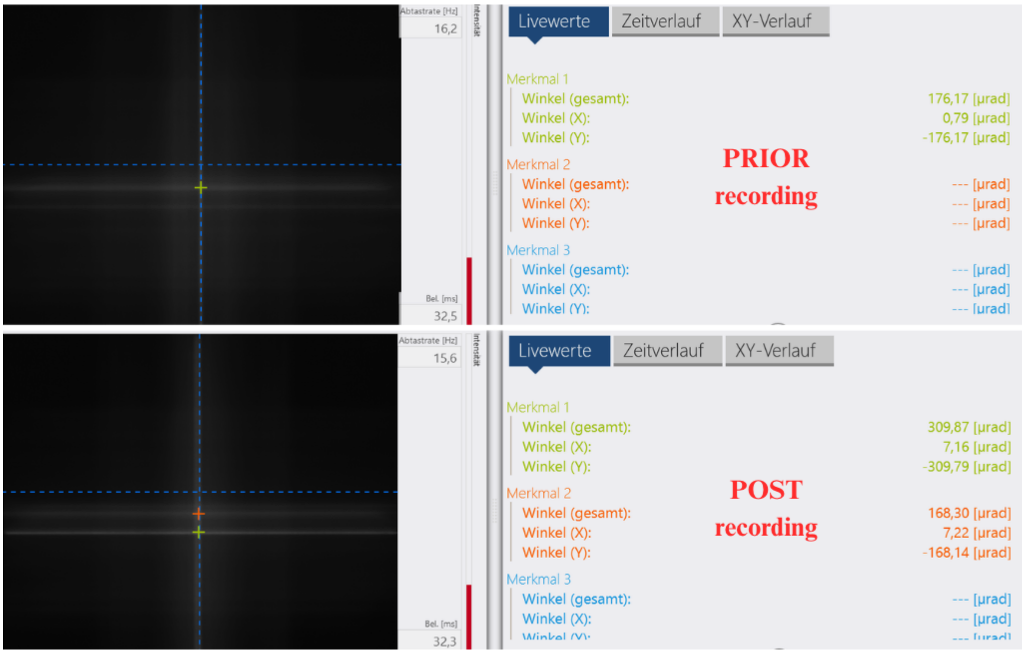

Figure 4.6.: Autocollimator readout of the angular alignment of grating G3. *Top panel*: Before holographic recording. *Bottom panel*: After holographic recording.

All NDPC gratings were successfully recorded over a diameter of approximately 25 mm. The final gratings (G1, G2 and G3) after sample fabrication and holographic recording are shown in the following images. When viewed under a suitable angle, the presence of the hologram is revealed by a distinct color variation across the grating area.

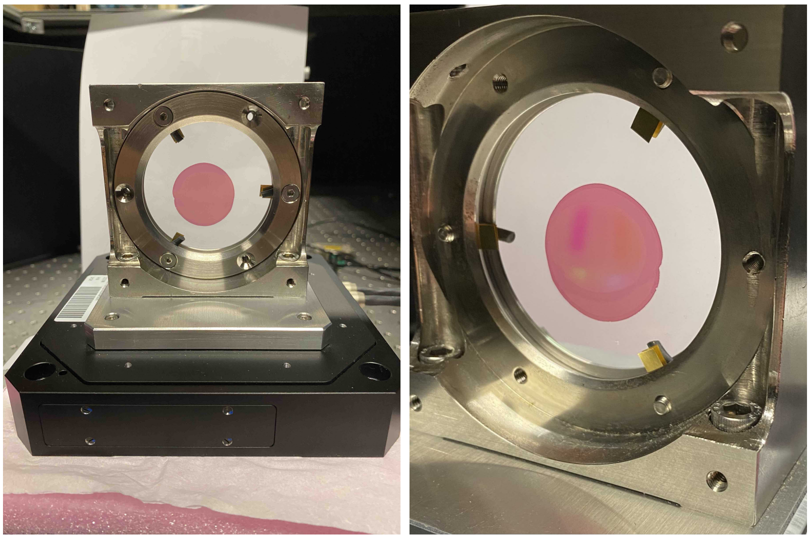

Figure 4.7.: Photograph of the final fabricated and recorded NDPC grating G1.
Left panel: Complete grating mounted in its holder (PI stage).
Right panel: Color gradient of the recorded hologram.

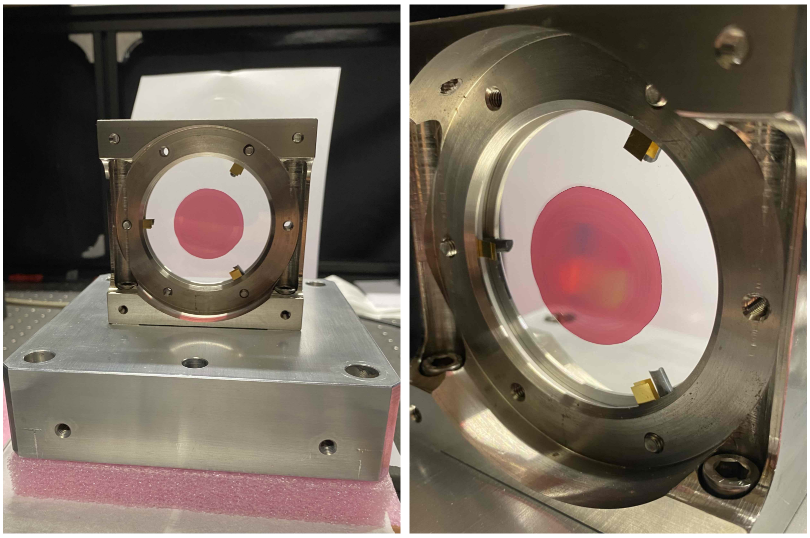

Figure 4.8.: Photograph of the final fabricated and recorded NDPC grating G2.
Left panel: Complete grating mounted in its holder (aluminium block).
Right panel: Color gradient of the recorded hologram.

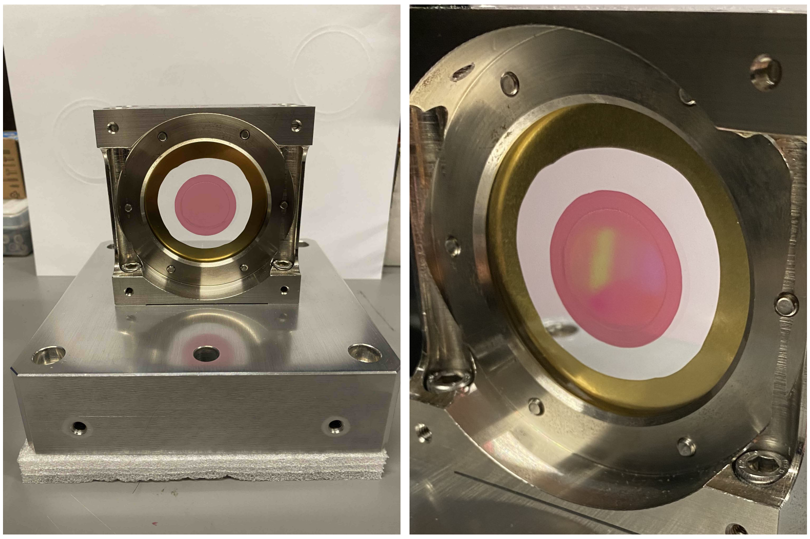

Figure 4.9.: Photograph of the final fabricated and recorded NDPC grating G3.
Left panel: Complete grating mounted in its holder (aluminium block).
Right panel: Color gradient of the recorded hologram.

The following images show the same NDPC grating (G3) photographed under slightly different viewing angles. The recorded hologram becomes visible as a characteristic color pattern, which changes with the viewing angle.

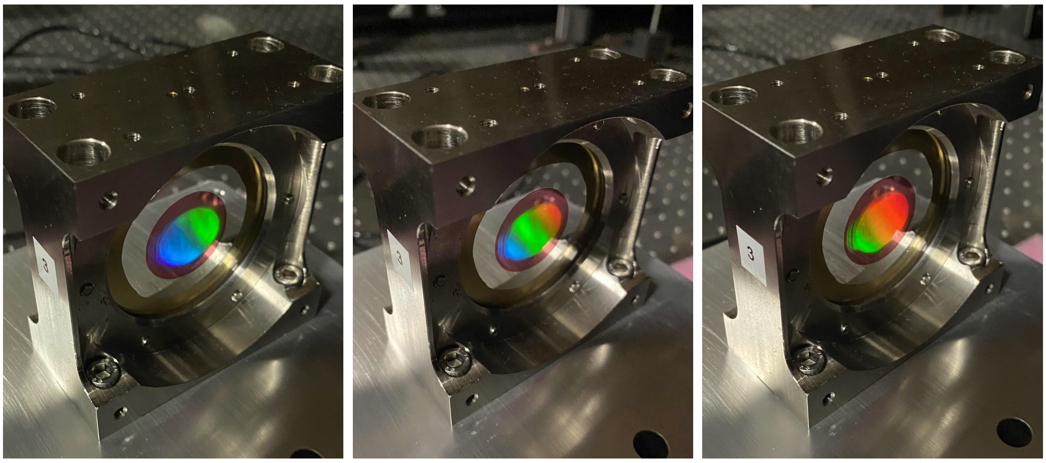

Figure 4.10.: Photographs of the same NDPC grating (G3) recorded under slightly different viewing angles, illustrating the angle-dependent appearance of the holographic color pattern.

4.2. Measured Rocking Curves of the NDPC Gratings

The following section presents the measured rocking curves of the fabricated holographic NDPC gratings, showing the diffraction efficiency $\eta(\Theta)$ as a function of the incident (external) angle Θ. The optical readout was performed using a green laser with a wavelength of $\lambda = 543.5\,\text{nm}$, in accordance with the procedure described in Chapter 3.3. For all gratings, the diffracted intensity of the -1st-order beam was measured. The probe beam was aligned to the center of the hologram. The grating parameters were extracted by fitting the measured rocking curve based on Uchida's coupled-wave model.

The figure below shows the rocking curve of grating G1 for the -1st diffraction order measured over an angular range from -40° to -25°.

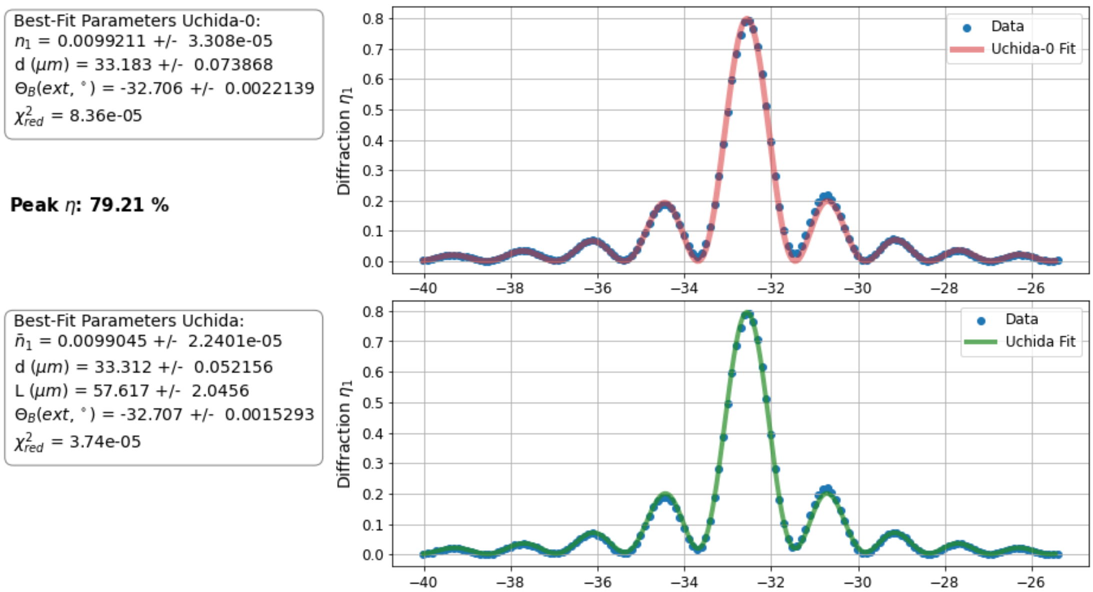

Figure 4.11.: Rocking curve of grating G1 for the -1st diffraction order. Blue points: Experimental data. Red curve: Uchida-0 model with n_1=const. Green curve: Uchida model with exponential decay of the refractive index modulation along the grating depth. Left side: Retrieved grating parameters.

In the rocking curve measurement above, the blue points represent the experimental data. The red curve in the upper panel corresponds to a fit based on Uchida's model assuming a constant refractive index modulation n_1 ("Uchida-0"), while the green curve in the lower panel shows the fit according to Uchida with an exponentially decaying refractive index modulation along the grating thickness $n_1(z)$, following Ref. [11]. In both cases, no absorption grating and no mean absorption were assumed. The retrieved grating parameters for both models are listed on the left, including the peak diffraction efficiency η, the (external) Bragg angle Θ_B and the effective grating thickness d. Note that the brass spacers define the nominal sample thickness d_0, but the actual thickness d of the recorded NDPC gratings may deviate slightly. In addition, the lower Uchida fit includes the decay length L accounting for attenuation of the refractive index modulation along the grating depth. The reported value of $\bar{n}_1$ denotes the mean refractive index modulation over the grating thickness (see Eq 2.17). Furthermore, the reduced chi-squared values (χ^2_{red}) are included in both cases as a quantitative measure of the fit quality, allowing for a direct comparison between the two fit models. It should be pointed out that the Bragg angle extracted from the rocking curve does not coincide exactly with the Bragg angle determined from the grating geometry. The actual Bragg angle Θ_B is obtained by measuring the $+1$ and the -1 diffraction orders of the same grating without removing or re-aligning the grating between measurements. Taking half of the sum of the absolute angular positions of the $+1$ and -1 diffraction maxima yields the corresponding Bragg angle. This results in $\Theta_B = 32.5°$ for a probing wavelength of 543.5 nm. The deviation seen in the plot above originates from the manual positioning of the grating during the readout procedure, leading to a constant angular offset. The quantitative evaluation is not affected, as the fit accounts for this offset. Using the retrieved Bragg angle of 32.5° at a wavelength of 543.5 nm and the Bragg condition (2.4) (with $m = 1$), the grating spacing can be calculated. This yields a grating period of $\Lambda = (505.7 \pm 1.4)$ nm for all gratings.

The figures below show the rocking curve measurements of grating G2 and G3 for the -1st diffraction order, taken over an angular range of -40° to -25°. Error bars are not shown, as the uncertainties of the optical measurement are smaller than the symbol size.

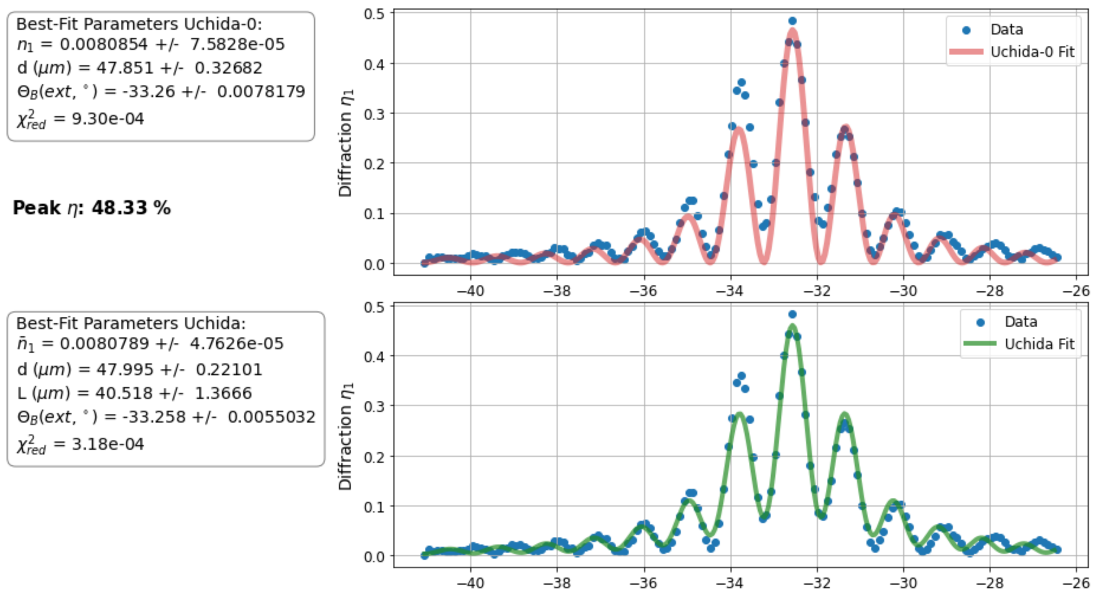

Figure 4.12.: Rocking curve of grating G2 for the -1st diffraction order. Blue points: Experimental data. Red curve: Uchida-0 model with n_1=const. Green curve: Uchida model with exponential decay of the refractive index modulation along the grating depth. Left side: Retrieved grating parameters.

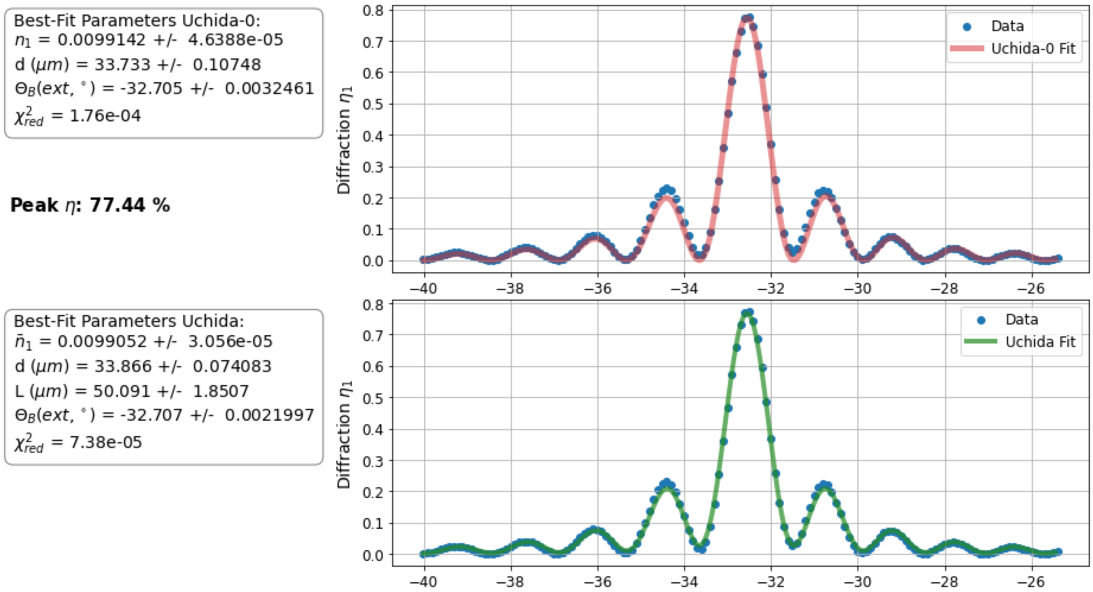

Figure 4.13.: Rocking curve of grating G3 for the -1st diffraction order. Blue points: Experimental data. Red curve: Uchida-0 model with n_1=const. Green curve: Uchida model with exponential decay of the refractive index modulation along the grating depth. Left side: Retrieved grating parameters.

The following table summarizes the retrieved grating parameters from the rocking curve measurements for gratings G1, G2 and G3.

Grating	Diffraction efficiency $\eta_{1,max}$	Refractive index modulation n_1	Grating thickness d [μm]	Decay length L [μm]	Coupling strength ν
G1	79%	9.904e-03 $\pm$ 0.022e-03	33.31 $\pm$ 0.05	57.62 $\pm$ 2.05	1.296 $\frac{\pi}{2}$ $\pm$ 0.004 $\frac{\pi}{2}$
G2	48%	8.079e-03 $\pm$ 0.047e-03	48.0 $\pm$ 0.2	40.52 $\pm$ 1.37	1.805 $\frac{\pi}{2}$ $\pm$ 0.013 $\frac{\pi}{2}$
G3	77%	9.905e-03 $\pm$ 0.030e-03	33.87 $\pm$ 0.07	50.1 $\pm$ 1.9	1.317 $\frac{\pi}{2}$ $\pm$ 0.006 $\frac{\pi}{2}$

Table 4.2.: Summary of the grating parameters for gratings G1-G3. The parameters were extracted from fits to the rocking curves shown in Fig. 4.11 4.12 4.13.

Table 4.2 lists the maximum diffraction efficiency $\eta_{1,max}$, the refractive index modulation n_1, the effective grating thickness d, the decay length L and the coupling strength ν. The maximum diffraction efficiency $\eta_{1,max}$ was obtained directly from the peak value of the measured rocking curve. The refractive index modulation n_1 and the effective grating thickness d were treated as free fit parameters, from which the coupling strength ν was calculated using Eq. (2.15). The uncertainties of the refractive index modulation n_1, the effective grating thickness d and the decay length L were obtained directly from the least-squares fitting procedure. The uncertainty of the coupling strength ν was determined by Gaussian error propagation. Error bars of the diffraction efficiency $\eta_{1,max}$ are omitted, as they are smaller than the data points.

The evolution of the refractive index modulation n_1 during the grating build-up as a function of recording time t for grating G1 is shown in the following.

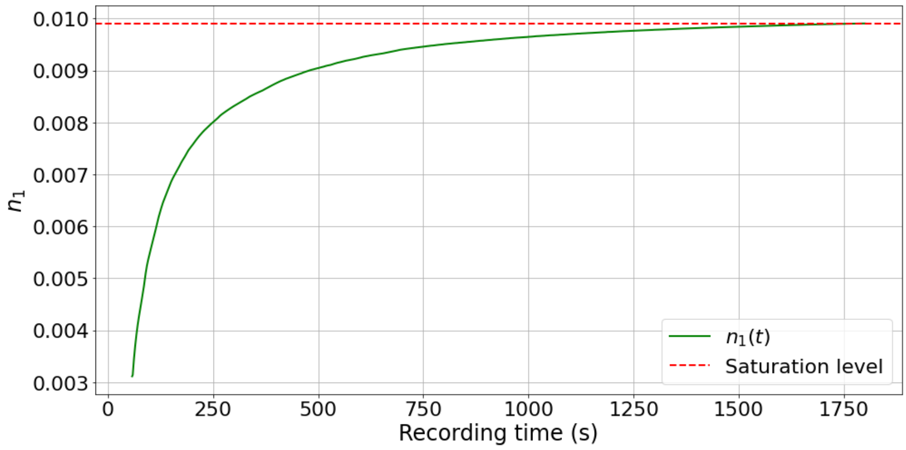

Figure 4.14.: Temporal evolution of the refractive index modulation $n_1(t)$ during grating buildup for grating G1. The plot starts at $t = 50\,\mathrm{s}$ to exclude the initial transient behavior. Saturation value $n_{1,sat} = 9.9e-3$.

The temporal evolution of the refractive index modulation $n_1(t)$ shown in Fig. 4.14 was reconstructed from the diffraction efficiency η measured at fixed Bragg incidence during the grating build-up process (see Fig. 4.1). During recording, the first-order diffraction efficiency $\eta(t)$ was monitored using a laser with a wavelength of 632.8 nm. The relation between diffraction efficiency and refractive index modulation (see Eq. 2.14 and 2.15) was inverted to obtain the temporal shape of $n_1(t)$. The saturation value of the refractive index modulation $n_{1,sat}$ was obtained independently from the rocking-curve measurements (see Fig. 4.11) and was used to fix the absolute scale of n_1. The data are plotted from $t = 50\,\mathrm{s}$ onward, as the initial grating buildup exhibits a transient behavior that is not representative of the steady growth regime.

To evaluate the lateral uniformity of the grating thickness, additional rocking-curve measurements were performed for each grating. For this purpose, the probe beam was positioned at a number of locations shifted by approx. 4-5 mm in different radial directions around the center. The corresponding measurements are presented in Appendix A.3. These measurements yield comparable values for the refractive index modulation n_1, peak diffraction efficiency $\eta_{1,max}$ and the effective grating thickness d.

4.3. Characterization of Additional NDPC Gratings

In the following, the results of the additionally fabricated NDPC gratings (C-PI, C-1, C2, C3) from the second fabrication run S15 are presented. Table 4.3 summarizes the extracted grating parameters for these gratings.

Grating	Diffraction efficiency $\eta_{1,max}$	Refractive index modulation n_1	Grating thickness d [μm]	Decay length L [μm]	Coupling strength ν
C-PI	39%	7.575e-03 ± 0.019e-03	52.92 ± 0.11	57.0 ± 1.3	1.575 $\frac{\pi}{2}$ ± 0.005 $\frac{\pi}{2}$
C-1	67%	5.937e-03 ± 0.031e-03	59.69 ± 0.24	51.67 ± 1.33	1.395 $\frac{\pi}{2}$ ± 0.009 $\frac{\pi}{2}$
C-2	41%	7.921e-03 ± 0.039e-03	53.18 ± 0.20	52.67 ± 2.26	1.656 $\frac{\pi}{2}$ ± 0.010 $\frac{\pi}{2}$
C-3	35%	8.128e-03 ± 0.034e-03	51.81 ± 0.16	48.6 ± 1.6	1.657 $\frac{\pi}{2}$ ± 0.009 $\frac{\pi}{2}$

Table 4.3.: Summary of the grating parameters for the additional NDPC gratings C-PI, C-1, C-2 and C-3 from sample set S15. The parameters were extracted from fits to the rocking curves shown in Fig. 4.15, 4.16, 4.17, 4.18

The measured rocking curves of all gratings are shown in the following Figures.

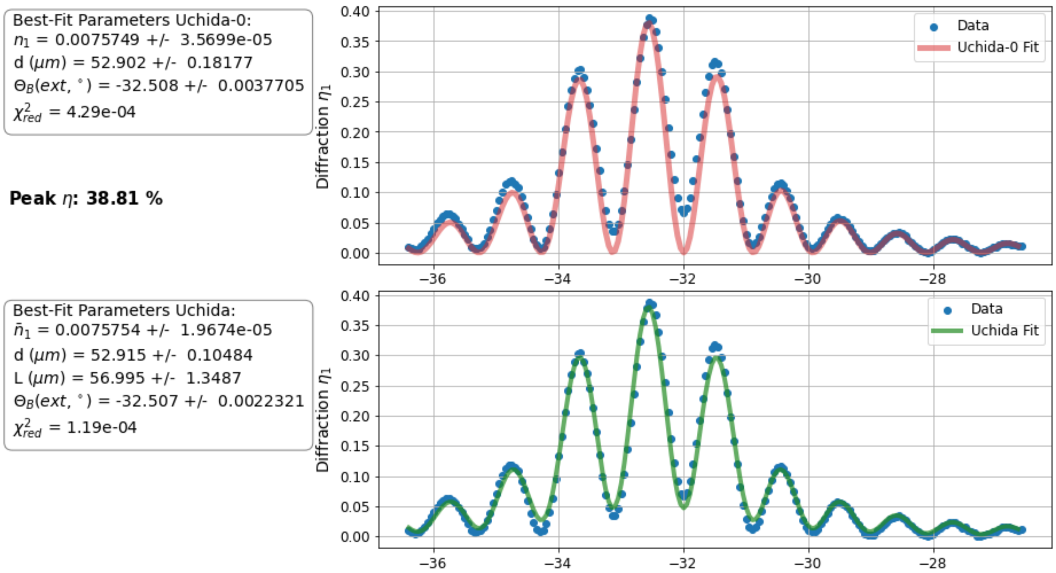

Figure 4.15.: Rocking curve of grating C-PI for the -1st diffraction order. Blue points: Experimental data. Red curve: Uchida-0 model with n_1=const. Green curve: Uchida model with exponential decay of the refractive index modulation along the grating depth. Left side: Retrieved grating parameters.

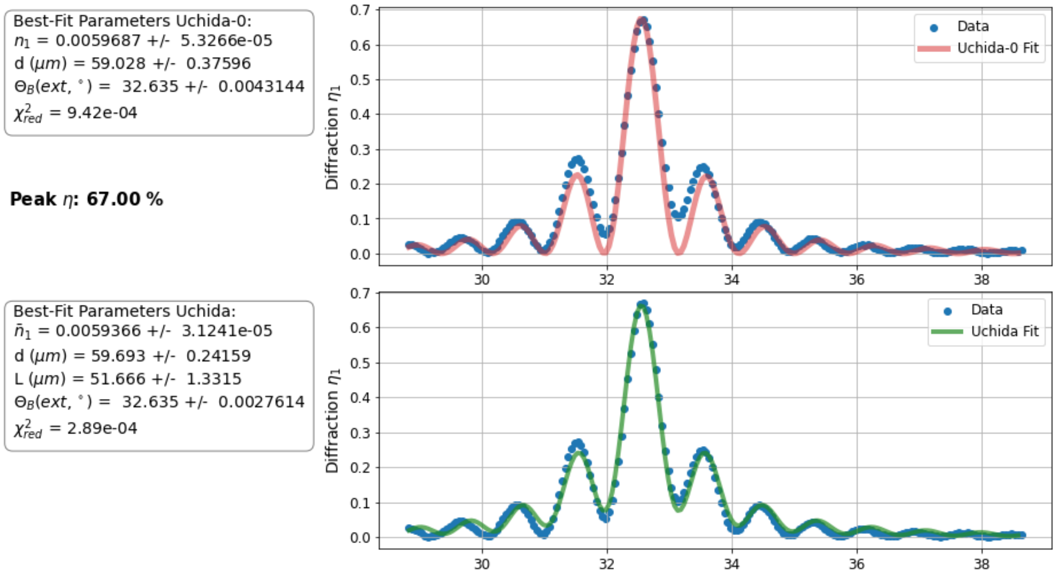

Figure 4.16.: Rocking curve of grating C-1 for the +1st diffraction order. Blue points: Experimental data. Red curve: Uchida-0 model with n_1=const. Green curve: Uchida model with exponential decay of the refractive index modulation along the grating depth. Left side: Retrieved grating parameters.

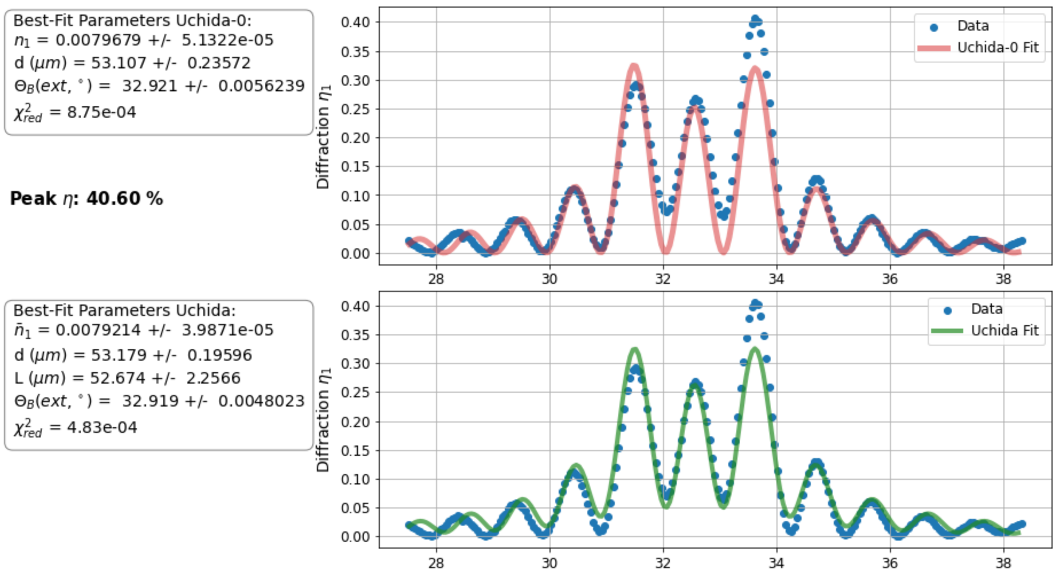

Figure 4.17.: Rocking curve of grating C-2 for the +1st diffraction order. Blue points: Experimental data. Red curve: Uchida-0 model with n_1=const. Green curve: Uchida model with exponential decay of the refractive index modulation along the grating depth. Left side: Retrieved grating parameters.

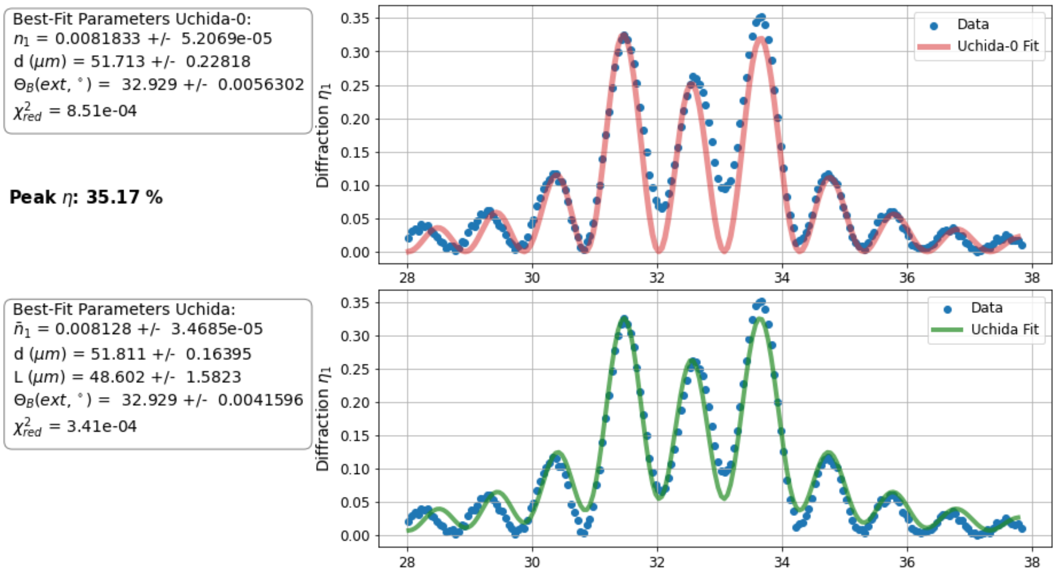

Figure 4.18.: Rocking curve of grating C-3 for the +1st diffraction order. Blue points: Experimental data. Red curve: Uchida-0 model with n_1=const. Green curve: Uchida model with exponential decay of the refractive index modulation along the grating depth. Left side: Retrieved grating parameters.

In summary, the optical characterization provides a consistent set of grating parameters for all investigated samples (G1, G2, G3 from the first fabrication run and C-PI, C-1, C-2, C-3 from the second fabrication run), which form the basis for the discussion of their suitability for neutron optical applications.

5. Discussion

In the following, the experimental results are discussed with respect to grating quality, homogeneity and their relevance for application in a neutron interferometer. The analysis includes the NDPC syrup preparation, temporal grating buildup and the measured rocking curves. Based on the extracted grating parameters, the gratings are evaluated with regard to their suitability as diffraction elements, acting as a mirror (G2) and as beam splitters (G1 and G3) in a LLL neutron interferometric setup. Additionally, the gratings fabricated in the second production run (C-PI, C-1, C-2 and C-3) are evaluated for their compatibility as beam splitters and mirrors, and are compared with gratings G1, G2 and G3 from the initial production process.

Overmodulation effects in holographic gratings

One recurring feature observed throughout the analysis is the occurrence of overmodulated gratings. Since this effect plays an important role in the interpretation of the grating buildup and diffraction efficiencies, it is briefly explained as follows [29]: Overmodulation in volume gratings can be explained within coupled-wave theory. The transmitted and first-order diffracted waves are coupled while propagating through the grating, resulting in a periodic exchange of energy along the grating thickness. For increasing coupling strength $\nu \propto n_1 \cdot d$, energy is transferred from the transmitted wave to the first-order diffracted wave and the diffraction efficiency initially increases. According to $\eta_1 = \sin^2(\nu)$, the first-order diffraction efficiency reaches its maximum at $\nu = \pi/2$ ($\eta_1 = 1$, i.e. 100%), corresponding to complete energy transfer into the first diffracted order. Once the coupling strength is $\nu > \pi/2$, the grating becomes overmodulated, meaning that energy is partially transferred back into the transmitted wave, resulting in a decrease of the first-order diffraction efficiency. In this context, due to the formal equivalence of light and neutron Bragg diffraction (see Eqs. 2.19 and 2.20), both diffraction efficiencies exhibit the same sinusoidal dependence on their respective coupling parameters. In the present NDPC material system, an increase in optical coupling strength has been observed to coincide with an increase in neutron diffraction efficiency (see Ref. [27]). However, this behavior depends on the value of the neutron coupling parameter. Consequently, an overmodulated grating is well suited to function as a neutron mirror, since a large fraction of the incident neutrons is diffracted. In contrast, a grating intended to act as a beam splitter requires a lower coupling strength of $\nu = \pi/4$, yielding equal intensities of the transmitted and diffracted neutron beams.

Temporal grating buildup during holographic recording

Beginning with the analysis of the grating buildup of gratings G1, G2 and G3, (as demonstrated in Figures 4.1, 4.2 and 4.3), all three gratings show the same characteristic temporal behaviour. The transient behaviour observed during the first approximately 50 seconds of grating formation can be explained by the fact that several processes take place in the material at the same time. At the very beginning, the diffusion of nanodiamonds and monomer molecules along the interference pattern causes a first weak grating to form, which results in an initial maximum of diffracted power. After about 10 seconds, this effect starts to level out and the diffracted intensity decreases again. Once this first phase has passed, the actual polymerisation process becomes dominant. Under continued illumination at high intensity, monomers start to cross-link, which leads to a slow but stable buildup of a polymer grating [30, 31]. This polymer grating creates a permanent refractive index modulation in the material. As a result, the diffracted power increases again and slowly approaches a final saturation. Grating G2 also shows a slight decrease in diffraction efficiency after reaching saturation, which is a first indication of an overmodulated grating. The different saturation times can be attributed to a misalignment of the red probe laser prior to recording. As a consequence, the probe beam used for monitoring the grating buildup in G1 was likely not incident exactly at the Bragg angle, leading to an apparently slower increase of the measured diffraction efficiency. For gratings G2 and G3, the probe laser was properly aligned at the Bragg condition, resulting in a faster apparent saturation. Despite the different buildup times, all gratings exhibit the same characteristic temporal behavior, indicating that the underlying syrup fabrication and the subsequent holographic recording process, including the recording geometry and physical mechanisms, were identical and functioned as intended.

Autocollimator based angular alignment of gratings

Regarding the alignment procedure monitored by the autocollimator, as can be seen in Images 4.4, 4.5 and 4.6, the measurements taken before and after holographic recording show no significant change for any of the three gratings, remaining within the permitted tolerance for angular deviations. Changes observed in individual autocollimator reflections ("Merkmale") during recording are most likely due to temporary effects, such as temperature-induced deformations caused by the $200\,\mathrm{mW/cm^2}$ recording laser intensity or mechanical stress. Therefore, given the use of an additional super-planar granite plate and grating holders of identical dimensions, no relevant changes in yaw, pitch or roll angles are expected to have occurred during the holographic recording process. Furthermore, no notable differences in yaw or pitch deviations are observed between gratings mounted on the PI stage (G1) and those mounted on the standard aluminium block (G2 and G3), indicating that both mounting approaches provide comparable alignment stability.

Assessment of grating quality based on visual observations

The consistent grating buildup and the small angular deviations provide a first indication of the successful fabrication of the holographic gratings. This is further supported by the large-area and visually homogeneous appearance of the recorded holograms (4.7, 4.8

and 4.9). Additionally, the observed angle-dependent color pattern in Image 4.10 can be attributed to the presence of a volume holographic grating. The absence of material clustering or NDPC syrup retraction confirms the homogeneous fabrication of all gratings, in contrast to effects observed in earlier fabrication runs (process S13, see Fig. A.2).

Analysis of the rocking curves

When examining the rocking curves of gratings G1, G2 and G3, it becomes evident that they exhibit the characteristic behavior of volume diffraction in the Bragg regime. Overall, the measured rocking curves are well described over the full angular range by both the Uchida-0 model without depth-dependent decay and the Uchida model including exponential decay of the refractive index modulation. The latter provides only a slightly better description of the rocking curves, which is reflected by the marginally smaller reduced chi-squared values obtained for the Uchida model compared to the Uchida-0 model. This indicates that any depth-dependent decay of the refractive index modulation is negligible for the investigated gratings. Thus, no significant differences are observed in the extracted parameters, as both Uchida models yield very similar values for the refractive index modulation and the effective grating thickness. Regarding the individual rocking curves and the corresponding fit parameters, the three gratings can be compared as follows.

Grating G1 (see Fig. 4.11) shows a largely symmetric rocking curve characterized by a single pronounced maximum at the Bragg angle and weak secondary maxima, with minima approaching zero. Of all three gratings, G1 exhibits the highest diffraction efficiency, reaching approx. 79% for the probing laser at 543.5 nm. At a wavelength of 632.8 nm, a diffraction efficiency of approx. 80% is obtained. Using Eq. 2.20, the analytically calculated diffraction efficiency is approx. 97%. The deviation between these values is attributed to a slight misalignment of the red probe laser during grating buildup, resulting in off-Bragg probing, and to the fact that the grating is already operating in the overmodulated regime at 632.8 nm. This interpretation is consistent with the previously observed grating buildup behavior. G1 reaches a refractive index modulation of 0.0099, which is close to the target value of $n_{1,sat} \geq 0.01$. Although a nominal thickness of 25 μm was intended, an effective grating thickness of 33.31 μm was obtained. While this deviation is still considered acceptable, it indicates a reduced thickness control at this thickness scale. With respect to the coupling strength, defined by n_1 and d, a value of $\nu = 1.296\frac{\pi}{2}$ for a wavelength of 543.5 nm is obtained. Although this value indicates slight overmodulation, the increased coupling strength results in an enhanced neutron diffraction efficiency, allowing the grating to operate close to the beam splitter condition. The extracted decay length $L = 57.61\,\mu$m is significantly larger than the effective grating thickness, indicating that the refractive index modulation can be considered approximately uniform over the grating depth. Consequently, grating G1 fulfils the requirements to serve as a beam splitter in a VCN interferometer, providing sufficient diffraction efficiency and good grating parameters.

The rocking curve of **grating G2** (see Fig. 4.12) exhibits a distinctly different behavior compared to grating G1. In agreement with the grating buildup behavior, which already indicated overmodulation, the rocking curve shows characteristic features of an overmodulated grating. These include a suppressed main maximum at the Bragg angle and pronounced secondary maxima. The elevated minima are attributed to the large effective grating thickness and additional nonlinear effects, for instance holographic scattering. In addition, a slight asymmetry of the rocking curve is observed. The diffraction efficiency of the secondary maxima on the left side of the Bragg angle is systematically higher than that on the right side. This asymmetry likely originates from non-linearities of the grating. Both the Uchida-0 model without decay and the Uchida model including an exponential decay reproduce the overall shape of the rocking curve reasonably well. However, the latter provides a slightly improved description of the experimental data, particularly with respect to the lifted minima. Despite these differences in fit quality, the extracted grating parameters remain similar for both models. While grating G2 reaches a maximum diffraction efficiency of approx. 88% for the red probe laser, a significantly lower value of approx. 48% is obtained for the green laser wavelength, which is the lowest among the three gratings. This difference arises from the wavelength dependence of the coupling strength, as the effective grating strength scales inversely with the probe wavelength. Consequently, the strong coupling at the green and red wavelength leads to overmodulation, causing a reduction of the first-order diffraction efficiency due to back-transfer of energy to the transmitted beam. This is in agreement with the overmodulated behavior observed previously. For grating G2, the refractive index modulation reaches a value of 0.0081, which is the lowest among the three gratings, but still close to the target value $n_{1,sat}$. The grating was designed with a nominal thickness of $50\,\mu$m and an effective grating thickness of $48.0\,\mu$m was obtained from the fit, corresponding to a deviation of only about 4%. This deviation lies well within the acceptable range and thus confirms good control over the grating thickness during fabrication. The coupling strength reaches a value of $\nu = 1.805\frac{\pi}{2}$ (for $\lambda = 543.5\,$nm), which is the highest among all investigated gratings and clearly indicates strong overmodulation. This is expected, as G2 has the largest effective grating thickness and the coupling strength increases linearly with the thickness. Owing to the high neutron diffraction efficiency associated with such strong optical coupling, the grating is well suited to serve as a mirror in a neutron interferometric setup, where a large fraction of the incident neutron beam is diffracted. The extracted decay length is $L = 40.52\,\mu$m and is slightly smaller than the effective grating thicknes, indicating that the refractive index modulation is not homogeneous along the entire grating depth. Such a depth-dependent modulation can result from light attenuation and depth-dependent polymerization effects during recording. Overall, the optical properties of grating G2 are well suited for its intended use as a mirror element in a VCN interferometer.

For the third **grating G3** (see Fig. 4.13), both the rocking curve and the extracted fit parameters show behavior similar to that of grating G1. Like G1, grating G3 exhibits a largely symmetric rocking curve with a pronounced maximum at the Bragg angle, weaker side lobes and minima reaching zero. The maximum diffraction efficiency, which G3 reaches, amounts to 77% at a the green probing wavelength and 82% at the red wavelength. An analytical calculation (using Eq. 2.20) yields a higher value of approxim.

95%, resulting again from slight misalignment of the red probe laser relative to the Bragg condition. Grating G3 reaches a refractive index modulation of 0.0099, which is again close to the target value $n_{1,sat}$ required for efficient diffraction and comparable to that of grating G1. The grating was fabricated with a nominal thickness of 25 μm and exhibits an effective grating thickness of 33.87 μm, which is nearly identical to that of G1. The coupling strength reaches a value of $\nu = 1.317\frac{\pi}{2}$ for a wavelength of 543.5 nm, indicating a slightly overmodulated grating. However, similar to grating G1, this increased coupling strength corresponds to an enhanced neutron diffraction efficiency. The decay length $L = 50.09\,\mu$m is larger than the effective grating thickness, implying that depth-dependent attenuation of the refractive index modulation is negligible for this grating. Overall, grating G3 meets the criteria for use as a second beam splitter in the LLL neutron interferometer setup.

Buildup dynamics of the refractive index modulation in grating G1

Looking at the temporal evolution of the refractive index modulation (see Fig. 4.14) during the grating buildup of grating G1 and considering the buildup behaviour from $t = 50$ s onward, it can be observed that the refractive index modulation approaches saturation after approximately 1500 s. This indicates that a recording time of 1800 s is a well chosen duration for the holographic recording process. Terminating the exposure earlier would likely result in a slightly reduced grating quality, even though the polymerization process would presumably continue after the end of the recording. The initial rapid increase of the refractive index modulation agrees with the fast rise of the diffraction efficiency at the beginning of the recording process. This behaviour is caused by a rapid polymerization at early times, followed by a slower, diffusion limited growth that leads to the saturation of both the refractive index modulation and the diffraction efficiency.

Assessment of lateral grating homogeneity

The off-centre rocking curve measurements presented in Appendix A.3 confirm the lateral homogeneity of the three NDPC gratings. For grating G1, the off-centre rocking curves show very similar behaviour to the central measurement, with only minor variations in the extracted parameters. The refractive index modulation ranges from 0.0087 to 0.0093 compared to the central value of 0.0099, while the effective grating thickness remains nearly constant at approximately 33.3 μm. For grating G2, slight differences in the rocking curve shape are observed at off-centre positions, with reduced primary maxima indicative of strong overmodulation. Nevertheless, the extracted parameters remain consistent, with refractive index modulation around 0.0084 compared to 0.0080 at the centre and an effective thickness close to the central value of about 48 μm. For grating G3, the off-centre refractive index modulation varies between 0.0089 and even 0.010, slightly exceeding the central value of 0.0099, while the effective thickness remains close to 34 μm. Overall, the results demonstrate a laterally homogeneous refractive index modulation and grating thickness across all investigated gratings. The gratings can therefore be regarded as large-area, optically homogeneous diffraction elements suitable for use in an LLL neutron interferometer.

Comparison of gratings from the first and second fabrication runs

The additional NDPC gratings fabricated in the second production run, C-PI, C-1, C-2 and C-3, can be directly compared to gratings G1–G3 from the first run. Analysis of the rocking curves (see Figs. 4.15, 4.16, 4.17, 4.18) shows that all of these gratings exhibit overmodulation, which is consistent with the extracted fit parameters. The gratings reach diffraction efficiencies between 35% and 67%, which are lower than those of G1–G3. With the exception of C-1, the gratings from the second run are close to the targeted thickness of $50\,\mu$m and show smaller deviations from the nominal value than gratings G1–G3. The refractive index modulation is around 8×10^{-3} for all gratings except C-1, which exhibits the lowest value of all samples with 0.006. Gratings C-PI, C-2 and C-3 show high coupling strengths between $1.575\frac{\pi}{2}$ and $1.657\frac{\pi}{2}$ (at $\lambda = 543.5\,$nm), reflected in a partially suppressed central maximum and pronounced side lobes. Overall, the gratings from the second fabrication tend to be more strongly overmodulated than those from the first run, as expected for this thickness range. Ultimately, the gratings from the second fabrication run demonstrate improved control over the target thickness, likely due to the improved clamping rings (see Fig. 3.12), while the first run shows superior material quality in terms of refractive index modulation. A plausible explanation is deviations of the component weights from the intended composition, aging of the ND sol prior to sample preparation or nonoptimal evaporation times in the vacuum chamber, which can significantly affect the material quality and may have contributed to the reduced refractive index modulation for the second fabrication run. In conclusion, these gratings exhibit suitable parameters for application as neutron optical elements in an LLL interferometer.

Suitability of the NDPC gratings for VCN interferometry

The optically determined grating parameters indicate that the fabricated NDPC gratings meet the key requirements for VCN interferometry. For very cold neutrons, the optimal grating thickness is determined by the relation $d \propto \Lambda^2/\lambda$ [30]. For a neutron wavelength of about 5 nm and a grating period of approximately 500 nm, this yields an optimal thickness of around $50\,\mu$m, which is closely matched by the effective thicknesses of all investigated gratings. Thicker gratings would increase angular and wavelength selectivity. Since VCN beams exhibit a relatively broad wavelength distribution, only a fraction of the spectrum would fulfil the Bragg condition. The obtained thicknesses therefore represent a suitable compromise between diffraction efficiency and angular acceptance. Together with the grating period of 505.7 nm and the neutron wavelength, this leads to very small Bragg angles, as required for an LLL interferometer. For an interferometer length of $L = 1500\,$mm, this corresponds to a beam separation of approxim. 7.5 mm at the second grating. Such a separation requires a high degree of lateral homogeneity, which is confirmed by the consistent refractive index modulation and grating thickness measured at positions several millimetres off-centre. Overall, the results demonstrate that NDPC gratings with sufficient optical quality, lateral uniformity and mutual alignment can be reproducibly fabricated, providing a suitable basis for the implementation of an LLL neutron interferometer.

6. Summary and Outlook

The aim of this Master's thesis was the fabrication of large-area, homogeneous nanodiamond–polymer composite (NDPC) volume gratings suitable for use in a very cold neutron (VCN) interferometer in triple-Laue (LLL) geometry. For this purpose, three holographic gratings were successfully fabricated by preparing the required NDPC material, recording the gratings using a two-beam holographic recording setup and subsequently characterizing them by light optical diffraction measurements. Gratings G1 and G3 were designed to act as beam splitters, while grating G2 was intended to serve as a mirror. Optical characterization was performed by rocking curve measurements and analysed using coupled-wave theory, which allowed the determination of the diffraction efficiency, effective grating thickness, coupling strength and refractive index modulation. All three gratings show refractive index modulations close to the target value of $n_{1,sat} = 0.01$ and effective grating thicknesses of approximately $30\,\mu$m and $50\,\mu$m. The achieved grating parameters, including the grating period of about 505 nm, are well suited for neutrons with a wavelength of around 4.5 nm and meet the requirements for an LLL neutron interferometer. The measured lateral homogeneity shows that high-quality, large-area NDPC volume gratings were successfully fabricated. The gratings were fabricated with the aim of achieving highly parallel grating vectors in their recording position, which is essential for interferometric applications. Consequently, the achieved parameters allow the gratings to be used in their intended roles for very cold neutrons. In addition to gratings G1–G3, a second fabrication run was carried out, yielding four additional gratings with modified parameters. This second run was motivated by the need to better match the revised wavelength distribution of the VCN beamline. Consequently, a uniform target thickness of $50\,\mu$m was chosen for all gratings in this run. The extracted grating parameters demonstrate good optical quality, confirming that these gratings are suitable for use as optical elements in an LLL interferometer. Overall, the grating parameters obtained in both fabrication runs are close to the targeted grating parameter values.

The next step in this research is the transfer of the fabricated NDPC gratings to the PF2 VCN beamline at the Institut Laue-Langevin (ILL, Grenoble) and their integration into an LLL interferometer setup. This step has already been realized in a proof-of concept experiment at the ILL. Interferometric measurements with very cold neutrons allow the observation of interference phenomena and the determination of visibility and phase shifts. These measurements provide information on the coherence properties of the neutron beam and test the performance of the fabricated NDPC gratings in an LLL interferometer.

Bibliography

[1] H. Rauch. Neutronenoptik. In *Bergmann-Schaefer: Lehrbuch der Experimentalphysik, Band 3: Optik- Wellen- und Teilchenoptik*, chapter 13, pages 1161–1228. De Gruyter, Berlin, New York, 2004. doi:10.1515/9783110198041.1161.

[2] H. Rauch and S. Werner. *Neutron Interferometry: Lessons in Experimental Quantum Mechanics, Wave-Particle Duality, and Entanglement*. Oxford University Press, Oxford, United Kingdom, 2 edition, 2015. doi:10.1093/acprof:oso/9780198712510.001.0001.

[3] H. Rauch, W. Treimer, and U. Bonse. Test of a single crystal neutron interferometer. *Physics Letters A*, 47(5):369–371, 1974. doi:10.1016/0375-9601(74)90132-7.

[4] H. Maier-Leibnitz and T. Springer. Ein Interferometer für langsame Neutronen. *Zeitschrift für Physik*, 167(4):386–402, 1962. doi:10.1007/bf01378119.

[5] U. Bonse and M. Hart. An X-ray interferometer. *Applied Physics Letters*, 6(8): 155–156, 1965. doi:10.1063/1.1754212.

[6] C. Pruner, M. Fally, R. Rupp, R. May, and J. Vollbrandt. Interferometer for cold neutrons. *Nuclear Instruments and Methods in Physics Research Section A: Accelerators, Spectrometers, Detectors and Associated Equipment*, 560(2):598–605, 2006. doi:10.1016/j.nima.2005.12.240.

[7] J. T. Cremer. Neutron optics. In *Advances in Imaging and Electron Physics*, volume 172, chapter 5, pages 561–606. Elsevier, 2012. doi:10.1016/B978-0-12-394422-1.00005-0.

[8] M. Gruber, K. Eder, A. Zeilinger, R. Gähler, and W. Mampe. A phase-grating interferometer for very cold neutrons. *Physics Letters A*, 140(7-8):363–367, 1989. doi:10.1016/0375-9601(89)90068-6.

[9] G. Van der Zouw, M. Weber, J. Felber, R. Gähler, P. Geltenbort, and A. Zeilinger. Aharonov–bohm and gravity experiments with the very-cold-neutron interferometer. *Nuclear Instruments and Methods in Physics Research Section A: Accelerators, Spectrometers, Detectors and Associated Equipment*, 440(3):568–574, 2000. doi:10.1016/s0168-9002(99)01038-4.

[10] G. van der Zouw. *Gravitational and Aharonov-Bohm phases in Neutron Interferometry*. PhD thesis, Universität Wien, Austria, 2000.

[11] N. Uchida. Calculation of diffraction efficiency in hologram gratings attenuated along the direction perpendicular to the grating vector. *J. Opt. Soc. Am.*, 63(3):280–287, 1973. doi:10.1364/JOSA.63.000280.

[12] T. Neulinger, K. Bernert, P. Fierlinger, H. Filter, M. Hino, T. Jenke, F. Lapeyre, and O. Zimmer. Demonstration with very-cold neutrons of developments in Fourier time-of-flight. *Nuclear Instruments and Methods in Physics Research Section A*, 1066: 169570, 2024. doi:10.1016/j.nima.2024.169570.

[13] J. Heintze. *Lehrbuch zur Experimentalphysik. Band 4: Wellen und Optik*. Springer Spektrum, Heidelberg, Deutschland, 2017. doi:10.1007/978-3-662-54492-1.

[14] F. S. Chen, J. T. la Macchia, and D. B. Fraser. Holographic storage in lithium niobate. *Applied Physics Letters*, 13(7):223–225, 1968. doi:10.1142/9789812832047_0005.

[15] M. Fally. Diffraction theories for off-bragg replay: J.T. Sheridan's seminal work and consequences. *Asian Journal of Physics*, 32(5–8):319, 2023. doi:10.48550/arXiv.2411.13495.

[16] M. Fally. The photo-neutronrefractive effect. *Applied Physics B*, 75(4-5):405–426, 2002. doi:10.1007/s00340-002-1035-0.

[17] P. Hariharan. *Optical Holography: Principles, Techniques and Applications*. Cambridge Studies in Modern Optics. Cambridge University Press, 2nd edition, 1996. doi:10.1017/CBO9781139174039.

[18] H.-J. Eichler. Interferenz, Beugung und Wellenleitung. In *Optik: Wellen- und Teilchenoptik*, chapter 3, pages 301–480. De Gruyter, Berlin, New York, 2004. doi:10.1515/9783110198041.301.

[19] H. Kogelnik. Coupled wave theory for thick hologram gratings. *Bell System Technical Journal*, 48(9):2909–2947, 1969. doi:10.1002/j.1538-7305.1969.tb01198.x.

[20] J. Prijatelj, M.and Klepp, Y. Tomita, and M. Fally. Far-off-bragg reconstruction of volume holographic gratings: A comparison of experiment and theories. *Physical review. A, Atomic, molecular, and optical physics*, 87(6):063810, 2013. doi:10.1103/PhysRevA.87.063810.

[21] J.T. Sheridan. A comparison of diffraction theories for off-Bragg replay. *Journal of Modern Optics*, 39(8):1709–1718, 1992. doi:10.1080/713823578.

[22] M. Fally, J. Klepp, and Y. Tomita. An experimental study on the validity of diffraction theories for off-Bragg replay of volume holographic gratings. *Applied Physics B*, 108(1):89–96, 2012. doi:10.1007/s00340-012-5090-x.

[23] M. Fally, J. Klepp, C. Pruner, Hadden. E., A. Bianco, J. Kohlbrecher, H. Filter, T. Jenke, and Y. Tomita. Photosensitive materials for neutron optics. In *Photosensitive Materials and their Applications III*, volume 13015, page 130150O. SPIE, 2024. doi:10.1117/12.3022432.

[24] E. Hadden, M. Fally, Y. Iso, T. Jenke, J. Klepp, A. Kume, K. Umemoto, and Y. Tomita. Holographic nanodiamond–polymer composite grating with unprecedented slow-neutron refractive index modulation amplitude. *Applied Physics Letters*, 124(7): 071901, 2024. doi:10.1063/5.0186753.

[25] Y. Tomita, A. Kageyama, Y. Iso, K. Umemoto, A. Kume, M. Liu, C. Pruner, T. Jenke, S. Roccia, P. Geltenbort, et al. Fabrication of nanodiamond-dispersed composite holographic gratings and their light and slow-neutron diffraction properties. *Physical Review Applied*, 14(4):044056, 2020. doi:10.1103/PhysRevApplied.14.044056.

[26] P. Galli, R. Evans, C. Bertarelli, and A. Bianco. Cyclic allylic sulfide based photopolymer for holographic recording showing high refractive index modulation. *Journal of Polymer Science*, 59(13):1399–1413, 2021. doi:10.1002/pol.20210192.

[27] S. Falmbigl. Nanodiamond composite holographic gratings with high refractive index modulation. Master thesis, Universität Wien. (Unpublished).

[28] Physik Instrumente (PI) GmbH & Co. KG. *PZ195E User Manual: E-711/E-712 Modular Digital Multi-Channel Controller System*. Karlsruhe, Germany, February 2024. Version 2.4.0.

[29] S. Gallego, M. Ortuño, C. Neipp, C. García, A. Beléndez, and I. Pascual. Overmodulation effects in volume holograms recorded on photopolymers. *Optics Communications*, 215:263–269, 2003. doi:10.1016/S0030-4018(02)02244-7.

[30] S. Falmbigl, R. Ackermann, E. Hadden, H. Filter-Pieler, T. Jenke, J. Klepp, C. Pruner, Y. Tomita, and M. Fally. Application of nanodiamond-polymer composite holographic gratings in a very cold neutron interferometer. In *Holography: Advances and Modern Trends IX*, volume 13529, page 135290L. SPIE, 2025. doi:10.1117/12.3065648.

[31] M. Ellabban, G. Glavan, J. Klepp, and M. Fally. A comprehensive study of photorefractive properties in poly(ethylene glycol) dimethacrylate— ionic liquid composites. *Materials*, 10(1):9–9, 2016. doi:10.3390/ma10010009.

A. Appendix

A.1. Measurement Values

A.1.1. Syrup composition for sample set S13 (grating G3)

Component	Measured Weight (± 0.1) in mg
A-DPH	166.0
T-HFA	327.6
ND-sol	3160.8
RB	4.6
NPG	9.0
Total mass of syrup before evaporation	20347.4
Mass of remaining syrup after evaporation	17634.1

Table A.1.: Measured masses (in mg) of the chemical components used in sample set S13 and the resulting total mass of the syrup before and after the MIBK evaporation process. The uncertainty of all measured masses is ± 0.1 mg, corresponding to the readability of the analytical balance.

A.1.2. Syrup composition for sample set S14 (gratings G1 and G2)

Component	Measured Weight (± 0.1) in mg
A-DPH	162.2
T-HFA	338.0
ND-sol	3162.8
RB	4.3
NPG	8.5
Total mass of syrup before evaporation	20094.7
Mass of remaining syrup after evaporation	17380.0

Table A.2.: Measured masses (in mg) of the chemical components used in sample set S14 and the resulting total mass of the syrup before and after the MIBK evaporation process. The uncertainty of all measured masses is ± 0.1 mg, corresponding to the readability of the analytical balance.

A.1.3. Syrup composition for sample set S15 (gratings C-PI, C-1, C-2, C-3)

Component	Measured Weight (± 0.1) in mg
A-DPH	158.9
T-HFA	331.1
ND-sol	3157.2
RB	4.4
NPG	8.7
Total mass of syrup before evaporation	20912.8
Mass of remaining syrup after evaporation	18214.5

Table A.3.: Measured masses (in mg) of the chemical components used in sample set S15 and the resulting total mass of the syrup before and after the MIBK evaporation process. The uncertainty of all measured masses is ± 0.1 mg, corresponding to the readability of the analytical balance.

A.2. Alternative Sample Preparation S13

The following section describes the initial fabrication protocol used for sample set S13. This procedure proved less reliable for achieving homogeneous grating thicknesses and was therefore revised and replaced by the three-point-spacer-based method (S14) described in the main text. It is included here for completeness, since grating G3 was produced by this method. The procedure is shown in the images A.1.

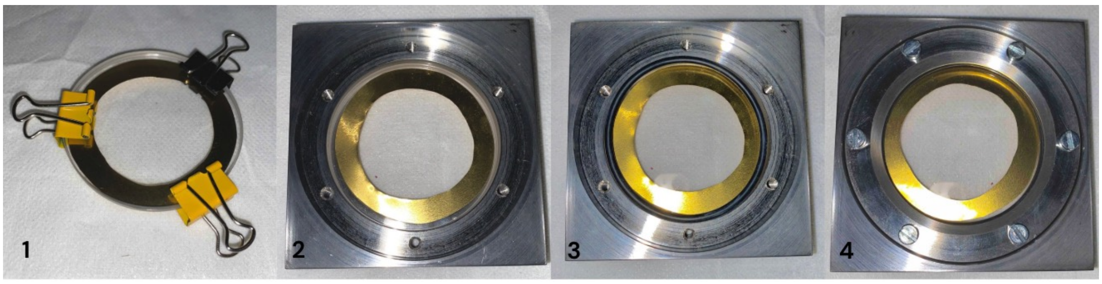

Figure A.1.: Step-by-step demonstration of the sample assembly (S13), shown without the NDPC syrup: 1. The ring-shaped brass spacer is placed between the two glass substrates, with the (hypothetical) NDPC syrup in between them. Clamps are pressed around the sample. 2. The substrate is inserted into the sample holder base. 3. The EPDM o-ring is placed on top 4. The clamping ring is placed and fastened, securing the full assembly.

In contrast to the S14 method, the S13 procedure involved preparing the samples first, followed by heating in an oven, and mounting them in the sample holders only after cooling. Instead of a three-point support, ring-shaped brass spacers were cut out. These spacers had an outer diameter of approximately 60 mm - 64 mm, corresponding to the glass substrate size, and an inner diameter of approximately 47 mm - 55 mm. The spacer ring was placed on the first glass substrate. Small drops of NDPC syrup were then added to the center, followed by placement of the second glass substrate on top, which was pressed onto the material until a homogeneous, circular layer was formed, similar to the S14 procedure. To ensure that the material did not contract again, three clamps were pressed around the glasses, pressing them together. These clamped samples were then placed in an oven at 80°C for 30 minutes. Once the assemblies cooled down, the clamps were removed and the finished samples were installed into their respective sample holders. Instead of the cut-up EPDM pieces, a complete EPDM O-ring (Angst + Pfister AG, Normatec Compound EPDM 70.00-02, inner diameter 59.36 mm, cross-section 3.00 mm) was placed on top of each upper substrate. Finally, a clamping ring was mounted on each holder, with each sample secured in place by tightening all six screws. The remaining steps of grating fabrication were identical to those of the S14 method.

The problem that occurred with this S13 method was, that the combination of the ring-shaped brass spacer, the complete EPDM O-ring and the clamping ring with all six screws induced stress, that caused the glass substrates to warp. Consequently, the material slowly retracted and could no longer be maintained as a uniform layer, resulting in the irregularities shown in the Figure below. Therefore, this procedure is not recommended. Instead, the procedure as performed in sample set S14 should be followed.

Figure A.2.: Fabrication failure from sample set S13, showing the retracted NDPC material between the two glass substrates.

A.3. Rocking Curves at Off-Center Beam Positions

The following plots show the rocking curve measurements for grating G1 in the external angular range from -38° to -28° at different positions approximately 5 mm away from the center. These measurements were performed to assess the lateral homogeneity of the grating, in particular by comparing the extracted values of the peak diffraction efficiency, the refractive index modulation n_1 and the real grating thickness d. This is particularly relevant for neutron interferometry, since the neutron beam exhibits a finite angular divergence and wavelength distribution. In addition, the two diffracted beams are laterally separated by approximately 7 mm at G2. Therefore, a laterally uniform grating is essential for consistent diffraction over the full beam cross section.

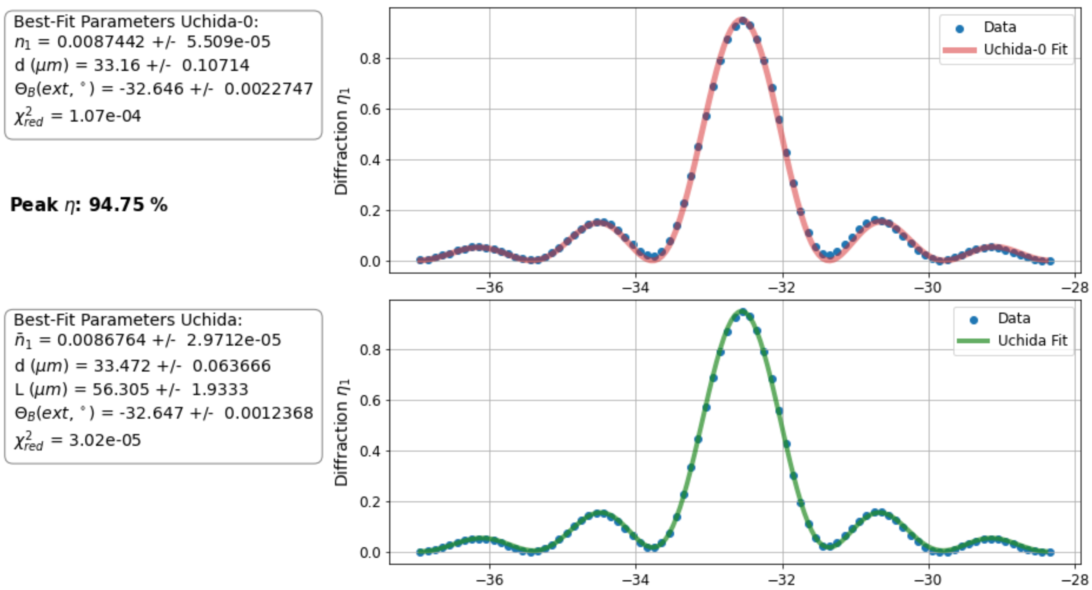

Figure A.3.: Rocking curve of grating G1 recorded at a position left of the center for the -1st diffraction order. Blue points: Experimental data. Red curve: Uchida-0 model with n_1=const. Green curve: Uchida model with exponential decay of the refractive index modulation along the grating depth. Left side: Retrieved grating parameters.

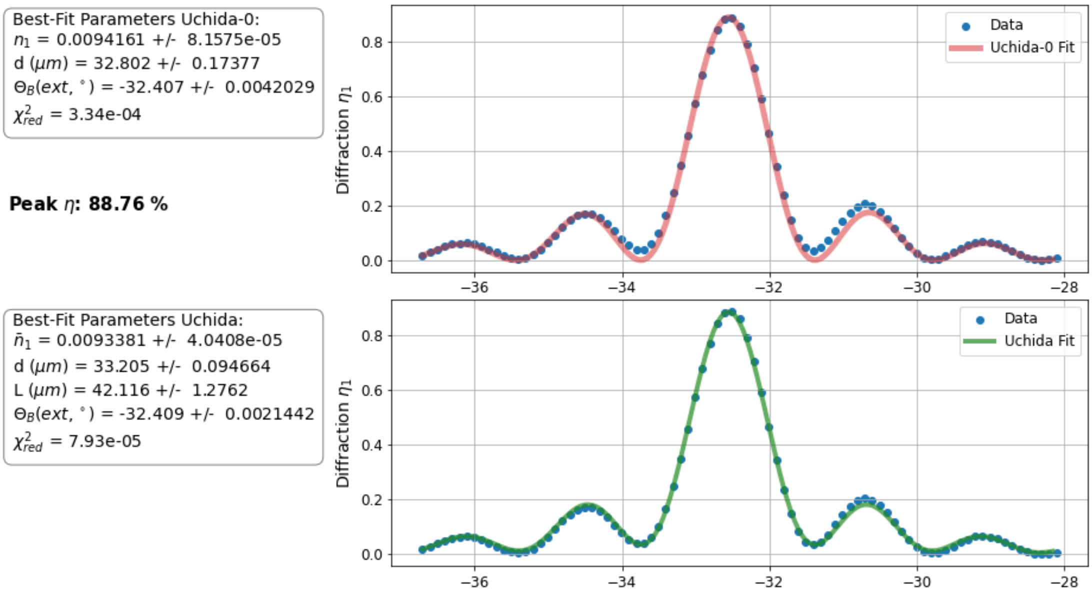

Figure A.4.: Rocking curve of grating G1 recorded at a position right of the center.

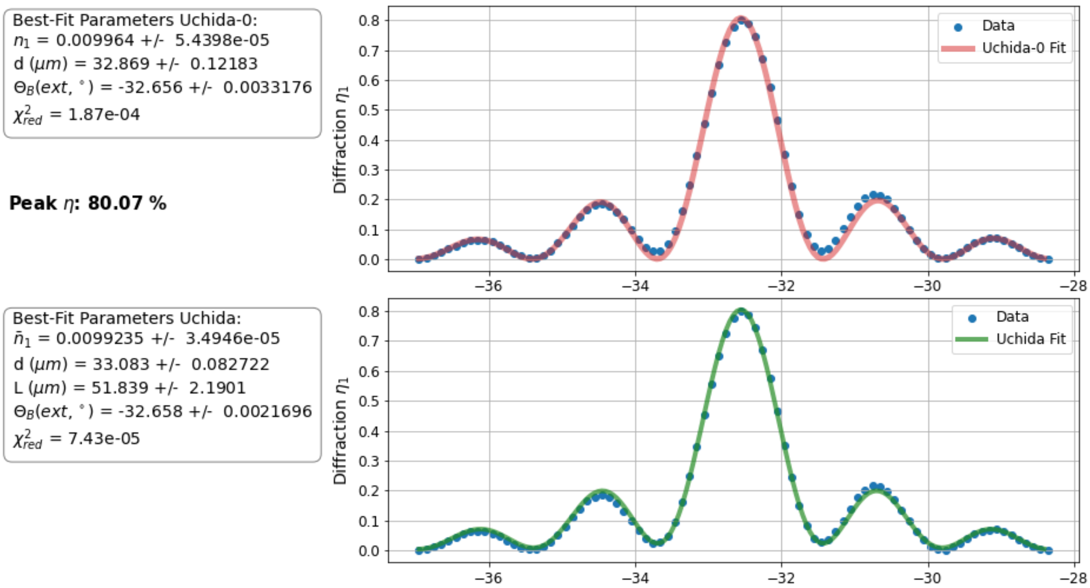

Figure A.5.: Rocking curve of grating G1 recorded at a position below the center.

The following figures show off-centre rocking curve measurements of grating G2.

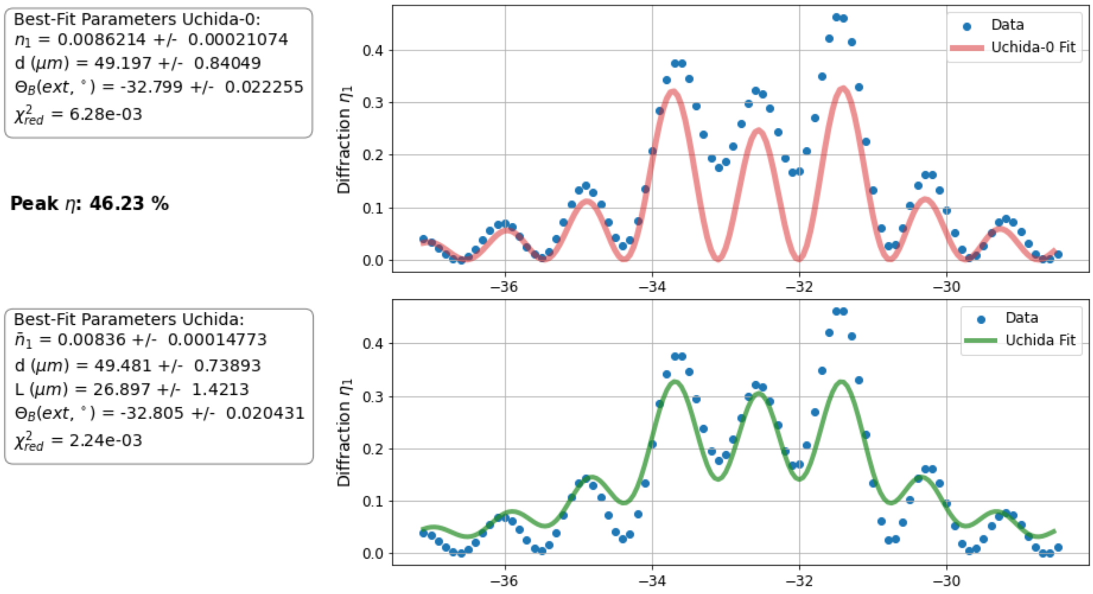

Figure A.6.: Rocking curve of grating G2 recorded at a position left of the center.

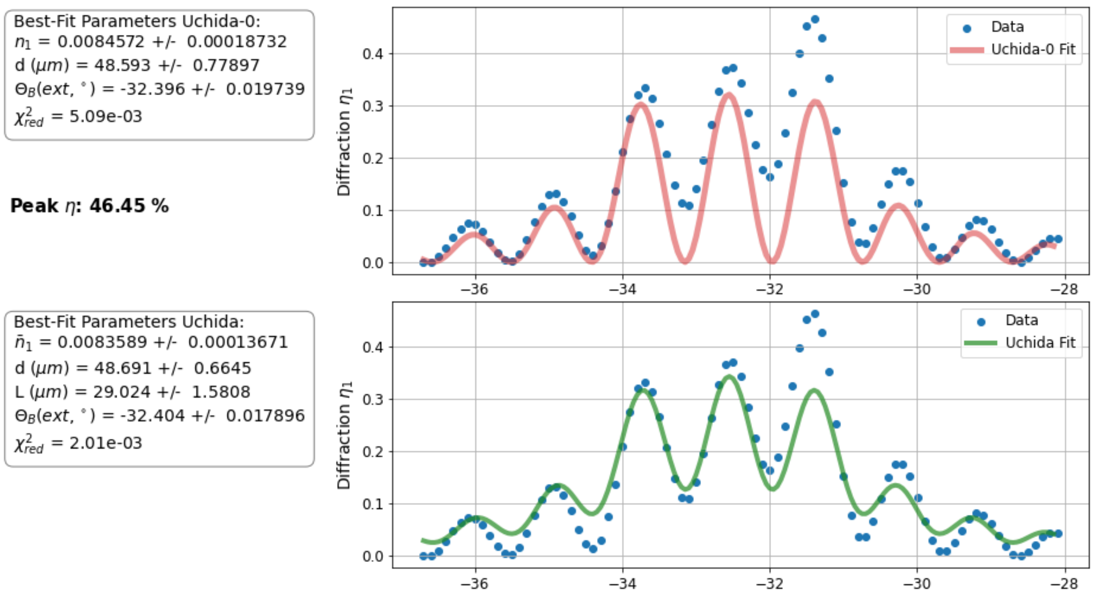

Figure A.7.: Rocking curve of grating G2 recorded at a position right of the center.

The off-centre rocking curve measurements for grating G3 are shown below.

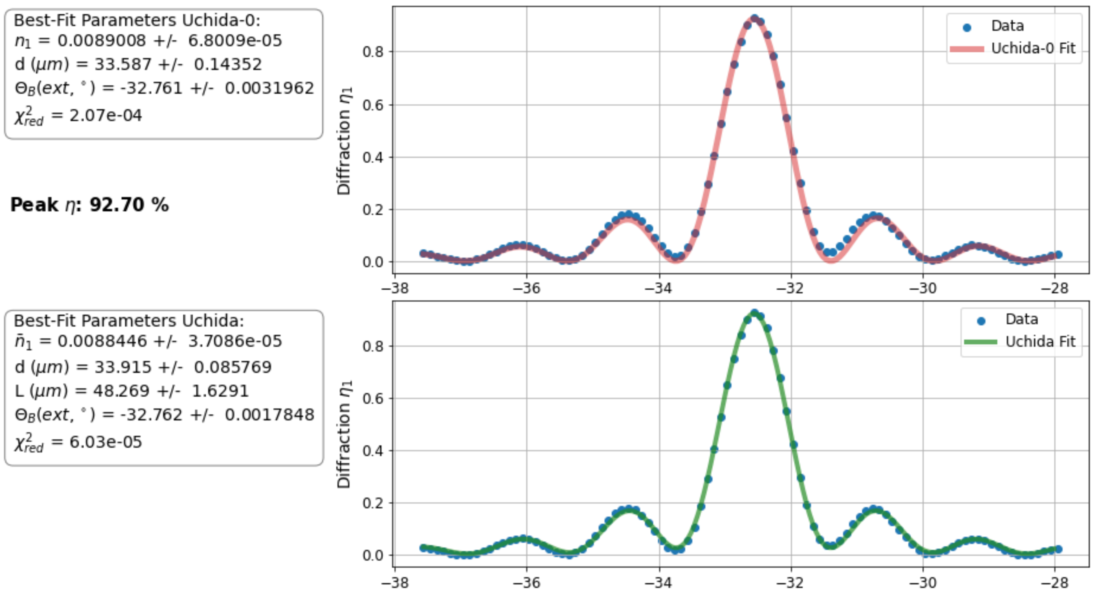

Figure A.8.: Rocking curve of grating G3 recorded at a position left of the center.

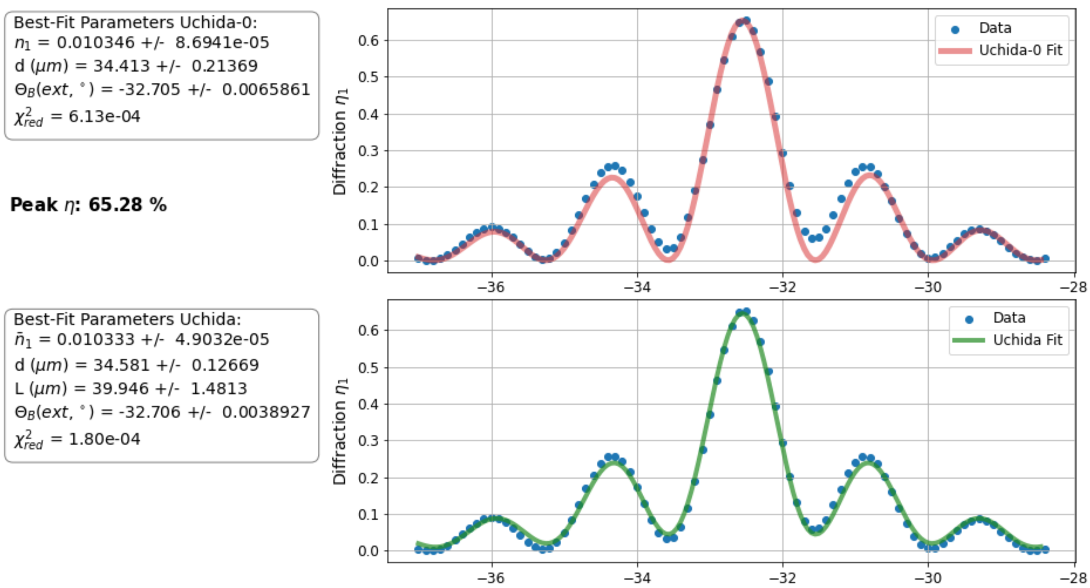

Figure A.9.: Rocking curve of grating G3 recorded at a position right of the center.

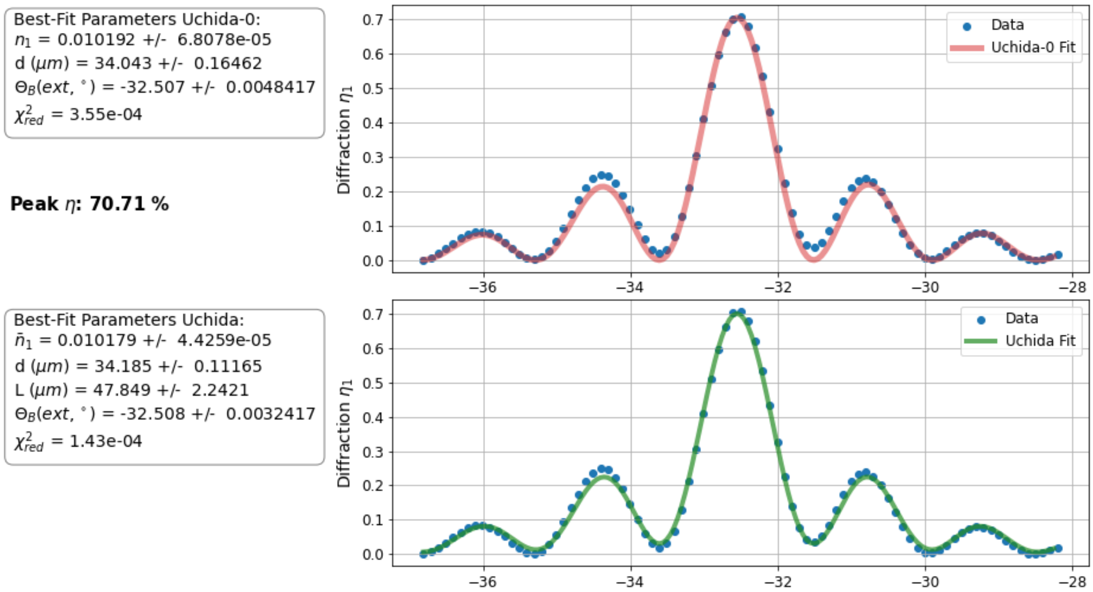

Figure A.10.: Rocking curve of grating G3 recorded at a position below the center.

The tables below present a summary of the extracted grating parameters, namely the peak diffraction efficiency $\eta_{1,max}$, the effective grating thickness d and the refractive index modulation n_1, for each grating, comparing measurements at the central and shifted positions.

Position	Diffraction efficiency $\eta_{1,max}$	Refractive index modulation n_1	Grating thickness d [μm]
Center	79.21%	9.904e-03 ± 0.022e-03	33.31 ± 0.05
Left	94.75%	8.867e-03 ± 0.029e-03	33.47 ± 0.06
Right	88.76%	9.338e-03 ± 0.041e-03	33.20 ± 0.09
Bellow	80.07%	9.923e-03 ± 0.035e-03	33.08 ± 0.08

Table A.4.: Comparison of extracted grating parameters at different lateral positions for grating G1.

Position	Diffraction efficiency $\eta_{1,max}$	Refractive index modulation n_1	Grating thickness d [μm]
Center	48.33%	8.079e-03 ± 0.047e-03	47.99 ± 0.22
Left	46.23%	8.360e-03 ± 0.021e-03	49.48 ± 0.74
Right	46.45%	8.359e-03 ± 0.013e-03	48.69 ± 0.66

Table A.5.: Comparison of extracted grating parameters at different lateral positions for grating G2.

Position	Diffraction efficiency $\eta_{1,max}$	Refractive index modulation n_1	Grating thickness d [μm]
Center	77.44%	9.905e-03 ± 0.030e-03	33.87 ± 0.07
Left	92.70%	8.844e-03 ± 0.037e-03	33.92 ± 0.09
Right	65.28%	10.333e-03 ± 0.049e-03	34.58 ± 0.13
Bellow	70.71%	10.179e-03 ± 0.044e-03	34.19 ± 0.11

Table A.6.: Comparison of extracted grating parameters at different lateral positions for grating G3.